

New Debris Disks Around Nearby Main Sequence Stars: Impact on The Direct Detection of Planets

C. A. Beichman¹, G. Bryden², K. R. Stapelfeldt², T. N. Gautier², K. Grogan², M. Shao², T. Velusamy², S. M. Lawler¹, M. Blaylock³, G. H. Rieke³, J. I. Lunine³, D. A. Fischer⁴, G. W. Marcy⁵, J. S. Greaves⁶, M. C. Wyatt⁷, W. S. Holland⁸, & W. R. F. Dent⁸

1) *Michelson Science Center, California Institute of Technology, Pasadena, CA 91125*

2) *Jet Propulsion Lab, 4800 Oak Grove Dr, Pasadena, CA 91109*

3) *Steward Observatory, University of Arizona, 933 North Cherry Ave, Tucson, AZ 85721*

4) *Department of Physics and Astronomy, San Francisco State University, San Francisco, CA 94132*

5) *Department of Astronomy, University of California, Berkeley, CA 94720*

6) *School of Physics and Astronomy, University of St. Andrews, North Haugh, St. Andrews KY16 9SS, UK*

7) *Institute of Astronomy, University of Cambridge, Cambridge, CB3 0HA, UK*

8) *UK Astronomy Technology Centre, Royal Observatory, Edinburgh EH9 3HJ, UK*

ABSTRACT

Using the MIPS instrument on the *Spitzer* telescope, we have searched for infrared excesses around a sample of 82 stars, mostly F, G, and K main-sequence field stars, along with a small number of nearby M stars. These stars were selected for their suitability for future observations by a variety of planet-finding techniques. These observations provide information on the asteroidal and cometary material orbiting these stars - data that can be correlated with any planets that may eventually be found. We have found significant excess 70 μm emission toward 12 stars. Combined with an earlier study, we find an overall 70 μm excess detection rate of $13 \pm 3\%$ for mature cool stars. Unlike the trend for planets to be found preferentially toward stars with high metallicity, the incidence of debris disks is uncorrelated with metallicity. By newly identifying 4 of these stars as having weak 24 μm excesses (fluxes $\sim 10\%$ above the stellar photosphere), we confirm a trend found in earlier studies wherein a weak 24 μm excess is associated with a strong 70 μm excess. Interestingly, we find no evidence for debris

disks around 23 stars cooler than K1, a result that is bolstered by a lack of excess around any of the 38 K1-M6 stars in 2 companion surveys. One motivation for this study is the fact that strong zodiacal emission can make it hard or impossible to detect planets directly with future observatories like the *Terrestrial Planet Finder (TPF)*. The observations reported here exclude a few stars with very high levels of emission, >1,000 times the emission of our zodiacal cloud, from direct planet searches. For the remainder of the sample, we set relatively high limits on dust emission from asteroid belt counterparts.

Subject headings: infrared: stars — circumstellar matter — Kuiper Belt

1. Introduction

A planetary system is characterized by the properties of its parent star, by the number and nature of its gas-giant and rocky planets, by the extent of its Kuiper and asteroid belts, and by the populations of gas and dust orbiting the central star. In the coming decade, astronomers will use a variety of techniques to address all these aspects of neighboring solar systems. Initial results for gas-giant planets are based on ground-based radial velocity searches. Eventually, nearby stars will be the targets of indirect and ultimately direct searches for terrestrial planets with the Space Interferometer Mission (SIM) and the Terrestrial Planet Finder (TPF). The *Spitzer* telescope is uniquely positioned to characterize the evolution, amount, structure and composition of the dust associated with Kuiper and asteroid belts around many types of stars, including those with and without the gas giant planets now being detected by the radial velocity technique. Guaranteed Time Observer (GTO) studies such as the FGK sample (Beichman et al. 2005b; Bryden et al. 2006a) and the Nearby Stars program (Gautier et al. 2006), plus the FEPS Legacy project (Meyer et al. 2004; Kim et al. 2005), have conducted photometric surveys of about 200 nearby stars at 24 and 70 μm . The photometric survey discussed here uses *Spitzer* images at 24 and 70 μm to look for debris disks around an additional 82 stars, rounding out existing surveys of the closest stars.

As the *Spitzer* programs are completed, we will be able to carry out statistical investigations of the debris disk phenomenon in terms of the age, metallicity, and spectral type of parent stars. In particular, by nearly doubling the size of the existing sample of stars (relative to the on-going GTO/Legacy programs) we can hope to identify and improve the statistics of types of excess that appear to be rare based on existing IRAS or ISO observations, e.g. hot dust, extremely large disk to star luminosity ratios ($L_{\text{dust}}/L_{\star}$) around mature stars (Fajardo-Acosta et al. 2000; Habing et al. 2001; Spangler et al. 2001),

or low mass stars. The incidence of excesses at the IRAS/ISO sensitivity level is about 15% (Backman & Paresce 1993; Bryden et al. 2006a) so that a total *Spitzer* sample of 250-300 stars can hope to identify over 50 stars with excesses suitable for future study. Stars with hot excesses (peak wavelength $< 24 \mu\text{m}$) are considerably rarer, 2-3% (Fajardo-Acosta et al. 2000; Laureijs et al. 2002; Beichman et al. 2006), so that a survey of a large number of stars is needed to generate a statistically meaningful sample.

As the statistics of planets build up, we will be able to correlate the properties of debris disks (total mass, physical configuration, composition) with properties of number, location, and mass of planets. Much lower dust masses can be detected with *Spitzer* than was previously possible, particularly for solar-type and cooler stars. Beichman et al. (2005b) and Bryden et al. (2006a) have shown that with *Spitzer* instruments, we can reach just a few times the fractional luminosity predicted for our own Kuiper Belt ($0.3 - 5 \times 10^{-6}$; Backman & Paresce 1993; Stern 1996). Determining how many mature stars like the Sun have Kuiper Belts comparable to our own is an important ingredient in understanding the formation and evolution of solar systems like our own (Levison & Morbidelli 2003).

Finally the *Spitzer* data will help us to understand the potential influence of zodiacal emission on the eventual direct detectability of planets. As highlighted in a number of TPF studies, including the *Precursor Science Roadmap for TPF* (Lawson et al. 2004), the level of exo-zodiacal emission can affect the ability of TPF to detect planets directly, particularly for extreme cases with much greater dust contamination than in the Solar System. A complete census of potential TPF stars will assist in the eventual selection of TPF targets by determining or setting a limit to the amount of exo-zodiacal emission around each star.

This paper focuses on the results of the $24 \mu\text{m}$ and $70 \mu\text{m}$ survey using the Multiband Imaging Photometer (MIPS) instrument on *Spitzer* (MIPS; Rieke et al. 2004). After describing our target selection (§2), we present these MIPS observations in §3. As will be discussed below, a number of sources in this sample appear to be extended. These are highlighted in §3, but are discussed in detail in a separate paper (Bryden et al. 2006b). Follow-up observations of sources with excesses using the IRS spectrometer are just now being completed; these will also be detailed in a later paper. In §4 we discuss how our MIPS flux measurements constrain the dust properties in each system. For the systems identified here as having IR excess, combined with those from Bryden et al. (2006a), §5 attempts to find correlations between the dust emission and system parameters such as stellar metallicity, spectral type, and age. Finally, in §6 we assess the influence of debris disks on the detectability of planets.

2. Stellar Sample

Our sample is based on work carried out by radial velocity search teams (e.g. Marcy et al. 2004) and by the SIM and TPF Science Teams to identify the most suitable targets for the indirect or direct detection of terrestrial-mass planets ($1-10 M_{\oplus}$). One target list consists of the 100 stars in the SIM Tier-1 sample which will be the most intensively observed stars in the two SIM projects dedicated to finding planets around nearby stars (Marcy et al. 2002; Shao et al. 2002).¹ Since the absolute astrometric signal from a planet scales as $3 \mu\text{sec} (D_{\star}/\text{pc})^{-1} \times (a_{\text{planet}}/\text{AU}) \times (M_{\text{planet}}/M_{\oplus}) \times (M_{\odot}/M_{\star})$, the SIM teams are concentrating on the some of the closest, lower mass stars for their deepest surveys for terrestrial planets. Thus, the SIM list includes a number of late K and M stars not included in the other *Spitzer* samples or in TPF lists.

We also draw from a number of lists prepared by Science Working Groups for the TPF-Coronagraph (TPF-C) and TPF-Interferometer (TPF-I) missions. Although the TPF lists are not definitive given the indeterminate status of the project, the outline of the sample is clear (Beichman et al. 2005c; Traub et al. 2006). We start with F0 - M5 stars of luminosity classes IV or V and refine the list by making a few simple assumptions about the nature of planetary systems and the properties of TPF. Specifically, we 1) exclude stars with binary companions within 100 AU as being inimical to the formation or stable evolution of planetary systems; 2) require that the angular extent of the habitable zone (Kasting et al. 1993); ~ 1 AU for a $1 L_{\odot}$ luminosity star, scaled by the square root of the stellar luminosity) exceed 50 milliarcsec; and 3) impose an outer distance cutoff of 25 pc (although we allowed a few F0-F5 stars at distances as great as 30 pc to bring up their numbers). To enable good measurements with *Spitzer* we rejected stars with high levels of stellar and/or cirrus confusion based on examination of IRAS maps.

Comparison of potential SIM and TPF targets in cirrus-free sky with the *Spitzer* Reserved Object Catalog (as of November 2003) showed 81 stars with spectral types ranging from F0 to M3.5, as listed in Table 1. One more star, GL 436, was added through a Director's Discretionary Time proposal after the discovery of a planet in this system was announced (Butler et al. 2004). Binary companions within the 82 fields of view have also been included as secondary targets; six such companions are identified as bright enough for clear detection in both the 24 and 70 μm images.² The divergent proper motion of HD 48682B, an M0 star

¹The merged, high priority target list for these projects is available at http://astron.berkeley.edu/~gmarcy/sim_draft.html.

²The 24 μm image of HD 265866 has what appears to be an equal-brightness binary companion located 40" NW of the target primary star. However, there is no visible or near-IR neighboring source. In fact,

30'' to the NE of HD 48682, rules out a physical association between the two stars. Thus, HD 48682B is not included in this sample. The true binarity of the other six neighboring sources is verified via their Hipparchos distances and space motion measurements. Angular separations in these systems range from 10'' to 100'', with projected orbital separations between 100 and 1000 AU. Data for the companions are listed separately at the end of Tables 1 and 2. With their inclusion, our total sample contains 88 stars within 82 targeted fields.

Binned by spectral type, the SIM/TPF sample consists of 37 F stars, 19 G stars, 24 K stars, and 8 M stars. Typical distances range from 10 to 20 pc, closer for M and K stars and farther for earlier spectral types. Figure 1 shows the overall distribution of observed spectral types. Some basic parameters of the sample stars are listed in Table 1, most importantly age and metallicity, which are also shown as histograms in Figures 2 and 3. There is no explicit target selection based on stellar age or metallicity, but known planet-bearing stars have been specifically included in a couple cases. Of this sample, only two stars (GJ 436 and HD 147513) are already known to have planets; most of the other stars with planets are either too faint, lie in cirrus-contaminated regions, or are already observed in other *Spitzer* programs (e.g. Beichman et al. 2005b).

In this paper we first discuss the 88 primary and secondary stars and then add in the stars observed in Bryden et al. (2006a) to increase the size of the sample for some of statistical discussions.

3. *Spitzer* Observations

All stars were observed with MIPS at 24 μm and, with one exception (HD 265866), at 70 μm . In order to help pin down their stellar photospheres, four M stars - GJ 908, HD 36395, HD 191849, and HD 265866 - were also observed with the IRAC camera in subarray mode at all four of its wavelengths (3.6, 4.5, 5.8, and 8.0 μm). Seven stars identified as having IR excess were observed with IRS, the *Spitzer* spectrograph, as follow-up observations, as detailed in a future paper.

the second 24 μm source is a chance alignment with a passing asteroid. Software specifically developed for locating asteroids relative to the *Spitzer* observatory (part of the Horizons package; Giorgini 2005) identifies this object as asteroid #11847 (“Winckelmann”: H=13.4, a=2.67 AU, e=0.065, i=10.23; Bowell 1996).

3.1. Data Reduction

3.1.1. MIPS Observations

Overall, our data analysis is similar to that previously described in Beichman et al. (2005b) and Bryden et al. (2006a). At $24\ \mu\text{m}$, images were created from the raw data using the DAT software developed by the MIPS instrument team (Gordon et al. 2005). At $70\ \mu\text{m}$, images were processed beyond the standard DAT software to correct for time-dependent transients, corrections which can significantly improve the sensitivity of the measurements (Gordon et al. 2004). For both wavelengths, aperture photometry was performed using apertures sizes, background annuli, aperture corrections, and instrument calibration as in Beichman et al. (2005b). We find that the target locations in the $24\ \mu\text{m}$ images are consistent with the telescope pointing accuracy of $<1''$ (Werner et al. 2004). As such, we use the $24\ \mu\text{m}$ centroid as the target coordinates for both wavelengths. Special consideration is made for the 6 resolved binaries in our sample. Instead of our standard method of aperture photometry with a surrounding sky annulus, the emission at the two stars' locations is fit with the instrument's point spread function (PSF). We find that for binary stars with small angular separations, simultaneously fitting of their overlapping PSFs results in much improved photometric accuracy. The agreement between PSF fitting and aperture photometry (with appropriate aperture correction) for isolated stars is excellent (Gordon et al. 2005). For all of the stars, the MIPS flux and noise measurements are listed in Table 2.

3.1.2. IRAC Observations

The IRAC sub-array images of the four M stars were reduced following the technique described by the FEPS Legacy team (Carpenter et al. 2006). The pixel sizes are corrected for distortion and a pixel-phase correction is made to channel 1. Stellar fluxes are measured within an aperture of 10 pixels ($=12''$), with a background annulus from 10 to 20 pixels. The photometric measurements each star at the four IRAC wavelengths are listed in Table 3.

3.2. Photospheric Extrapolations and Limits on $24\ \mu\text{m}$ Excess

To determine whether any of our target stars have an IR excess, we compare the measured photometry against predicted photospheric levels. A detailed description of our stellar atmosphere fitting, as applied to F5-K5 stars, is presented in the appendix of Bryden et al. (2006a). The stars observed here, however, span a greater range of spectral types than

previously considered. In particular, our sample contains late K and M type stars with numerous broad molecular features for which the stellar models (Kurucz 2003) begin to lose their accuracy.

This accuracy can be directly assessed by examining how well the observed flux levels match those predicted. We use the ratio, $F_{\text{MIPS}}/F_{*24\mu\text{m}}$, to assess the photospheric extrapolation using the fact previously established in Bryden et al. (2006a), Beichman et al. (2006), and earlier references cited therein, that excesses at $24\ \mu\text{m}$ are rare ($\sim 1\%$). Figure 4 shows the distribution of this ratio. After excluding one outlying star with a strong $24\ \mu\text{m}$ and $70\ \mu\text{m}$ excess (HD 109085), the 88 flux measurements at $24\ \mu\text{m}$ have an average $F_{\text{MIPS}}/F_{*24\mu\text{m}}$ of 1.01. The dispersion of $F_{\text{MIPS}}/F_{*24\mu\text{m}}$ in Figure 4 is 0.10, which is relatively large compared to the previous result for just F5-K5 stars (0.07; Bryden et al. 2006a). We identify three causes for this larger dispersion:

3.2.1. Quality of Near-IR Photometry

The SIM/TPF sample contains a number of nearby stars that are brighter than the stars in the FGK survey. Stars brighter than about $K_s = 4$ mag have saturated 2MASS measurements resulting in large photometric uncertainties (~ 0.25 mag). For several of these stars, particularly the early F type stars which are the brightest in the sample, Johnson K -band photometry is available in the literature with much better accuracy (~ 0.05 mag) than the saturated 2MASS values, but worse than the best 2MASS values (~ 0.03 mag). In such cases, the saturated 2MASS values are supplanted by the better data. However, the uncertainty in the near-IR photometry for the remaining 2MASS-saturated stars causes difficulty in extrapolating to longer wavelengths and results in a greater dispersion than when only stars with high quality 2MASS data are used, $\sigma(F_{\text{MIPS}}/F_{*24\mu\text{m}}) = 0.09$ vs. 0.07 for types F5-K5.

3.2.2. Intrinsic Variability

Stellar variability between the epochs of the Spitzer data and the photometry used to estimate the photospheric contribution could account for some of the dispersion in $F_{\text{MIPS}}/F_{*24\mu\text{m}}$. To investigate this possibility we examined the Hipparcos photometry for the 66 stars of our sample for which these data are available (ESA 1997). Only three stars (GL 436, HD 79211 and HD 265866) showed a scatter in $\text{mag}(Hp)$ in excess of 0.02 mag while the vast majority had scatter less than 0.01 mag. In particular, none of the ten stars younger than 1

Gyr and thus possibly more variable than the rest of the sample, showed variability above this level. GL 436 and HD 265866 are faint $V \sim 10$ mag M stars so that the level of Hipparcos scatter is not significant. The large scatter for HD 79211 (0.23 mag) is due to multiplicity and is also not significant. As discussed below, one non-Hipparcos star, HD 38392, shows a low level of variability and a correspondingly larger deviation in $F_{\text{MIPS}}/F_{*24\mu\text{m}}$.

3.2.3. Quality of Photospheric Models

The ability to extrapolate from visible and near-IR photometry to MIPS wavelengths appears to be an issue for spectral types later than the F5-K5 range used in the FGK survey. For all stars with accurate 2MASS data, Figure 5 plots the directly observable $K_s-[24]$ color, a quantity independent of the stellar atmosphere models. With the exception of the M stars, all of the averages are consistent with a constant color of $K_s-[24] \simeq 0.02 \pm 0.02$. Most interestingly, an apparently abrupt transition occurs between the late K stars and M stars, with the average $K_s-[24]$ color jumping up ~ 0.4 magnitudes for the cooler stars. This trend of redder $K_s-[24]$ for later spectral types was first noticed by Gautier et al. (2006) whose M star data are shown for comparison.

We next consider the ratio of the observed flux at $24 \mu\text{m}$ to that predicted by photospheric models ($F_{\text{MIPS}}/F_{*24\mu\text{m}}$) as a function of spectral type. Solar-like stars (types F5-K4) have an overall average of $F_{\text{MIPS}}/F_{*24\mu\text{m}} = 0.98 \pm 0.01$ with a dispersion of 5% among the stars with good 2MASS data and excluding stars with excess emission at $70 \mu\text{m}$ (identified in §3.3). For F0-F4 stars, the observed fluxes are marginally higher than those predicted, with an average $F_{\text{MIPS}}/F_{*24\mu\text{m}} = 1.03 \pm 0.02$. For late K stars with good 2MASS observations the observed fluxes are consistently below expectation with an average $F_{\text{MIPS}}/F_{*24\mu\text{m}}$ of 0.87 ± 0.03 . Since the observed K-[24] color is flat (Fig. 5), this offset is likely a fault of the photospheric modeling or of our fitting procedure. Not surprisingly, the models have the greatest difficulty with the M stars which have average $F_{\text{MIPS}}/F_{*24\mu\text{m}} = 1.16 \pm 0.06$. This difference between measured and predicted fluxes for the M stars remains even if NextGen (Hauschildt et al. 1999) models are used instead of Kurucz models. However, with an accurate determination of each star’s effective temperature and with more advanced stellar models (PHOENIX; Brott & Hauschildt 2005), Gautier et al. (2006) were able to fit the $24 \mu\text{m}$ colors of M stars.

Thus, knowing that these trends in $F_{\text{MIPS}}/F_{*24\mu\text{m}}$ exist and may ultimately be explained with better modeling, we can compare each star with the average $K_s-[24]$ color within its spectral type bin (Fig. 5) to look for dust excesses. With this methodology, we find no evidence for a $24 \mu\text{m}$ excess toward any of our M stars. This negative result is

strengthened when IRAC photometry is available. For the 4 M stars with IRAC data (Table 3), the inclusion of 3.5-8.0 μm fluxes into the fit modifies the average of $F_{\text{MIPS}}/F_{\star-24\mu\text{m}}$ from 1.32 with a dispersion of 0.21 to $F_{\text{MIPS}}/F_{\star-24\mu\text{m}}=0.92$ with a dispersion 0.04, confirming that the M stars' 24 μm fluxes are consistent with emission from the stellar photosphere alone.

3.2.4. Presence of a Weak Excess at 24 μm

Finally, the third reason for increased dispersion in the $F_{\text{MIPS}}/F_{\star-24\mu\text{m}}$ values, in addition to poor near-IR photometry and less accurate stellar photospheres or model fitting for late type stars, is the presence of weak but real excess emission from dust toward some stars. In §3.3 we will identify some of our target stars as having strong excess emission at 70 μm . Only one of these objects, HD 109085³ (the labeled value in Figure 4) also has an immediately obvious IR excess at 24 μm .

Taken in composite, however, the stars with 70 μm excesses tend to have a weak 24 μm excess. Considering only F0-K5 stars with good near-IR photometry, those with 70 μm excess have an average $F_{\text{MIPS}}/F_{\star-24\mu\text{m}}$ value 9% higher than those without. A similar general trend was previously noticed by Bryden et al. (2006a) and was confirmed in the IRS spectra of individual objects with 70 μm excess, which tend to rise above the stellar photosphere longward of 25 μm (Beichman et al. 2006). Combining the F0-K5 stars in this sample with those from Bryden et al. (2006a), we are no longer limited by small number statistics and the correlation between 70 μm and 24 μm excess becomes significant at the 3- σ level. The average 24 μm excess for stars with 70 μm excess is 0.079 ± 0.026 times the stellar flux.

To assess the significance of a possible 24 μm excess on a star-by-star basis, we define the parameter χ_{24} which corresponds to the $n - \sigma$ significance of any deviation from the expected photospheric value:

$$\chi_{24} \equiv \frac{F_{24} - F_{\star}}{\sigma_{24}} \quad (1)$$

where F_{24} is the measured flux, F_{\star} is the expected stellar flux, and σ_{24} is the noise level, all

³An excess was first detected around HD 109085 (= η Crv) by IRAS (Aumann 1988; Stencel & Backman 1991) and subsequently with SCUBA at sub-mm wavelengths (Sheret et al. 2004; Wyatt et al. 2005). Consistency between the IRAS flux at 25 μm and the MIPS 24 μm flux measured here depends strongly on the application of color corrections which are functions of the assumed dust temperature. For dust temperatures around 200-400 K and assuming the photospheric value given in Table 2, we find good consistency between the two measurements.

at 24 μm . A similar definition follows for 70 μm (equation [2]). We take the noise to be the larger of either 4% for sources with good 2MASS or Johnson data or 8% for sources with poor near-IR photometry. These values are based on the dispersions in $F_{\text{MIPS}}/F_{*}-24\mu\text{m}$ for the stars without 70 μm excesses. Ignoring the previously discussed late K and M stars with poor photospheric extrapolations, we find that the deviations from photospheric emission skew sharply to positive values for stars with 70 μm excess (*black shading* in Fig. 4). Using this analysis we identify statistically significant 24 μm excesses accompanying a stronger 70 μm excess around two stars: HD 25998 (3.6 σ) and HD 40136 (3.2 σ) in addition to HD 109085 discussed earlier. At slightly lower significance we find hints of a 24 μm excess for HD 199260 (2.7 σ) and HD 219482 (1.9 σ) which the accompanying 70 μm excess suggests could be real.

A number of other stars show strong deviations from photospheric values without an accompanying 70 μm excess: the deviant $F_{\text{MIPS}}/F_{*}-24\mu\text{m}$ values of the M stars have already been discussed and attributed to poor photospheric extrapolation; HD 38392 has an apparent 30% excess at 24 μm which we attribute to the difficulty of obtaining an accurate measurements due to a) saturated 2MASS measurements, b) proximity to a nearby, bright companion (HD 38393) and c) the possible variability of the star itself at the 5% peak-to-peak level (Nitschelm et al. 2000). Finally, HD 23249 and HD 55892 have $2 < \chi_{24} < 3$ and $\chi_{70} < 2$. These deviations could simply be statistical fluctuations or they could be hints of an excess like that seen toward HD 69830 which is prominent only in the 8-34 μm region but not at 70 μm (Beichman et al. 2005a). Without additional data, e.g. IRS spectra, we cannot assess the reality of the excesses around these last two stars.

3.3. Detection of 70 μm Excess

Having used 24 μm fluxes to test the accuracy of our stellar photosphere predictions, we next consider the frequency and strength of excess emission at 70 μm . The distribution of 70 μm flux densities relative to the expected photospheric values is shown in Figure 6. Unlike the tight distribution of flux ratios at 24 μm , many stars have 70 μm flux densities much higher than expected from the stellar photosphere alone. In several cases, the flux is more than an order of magnitude greater than expectation. Twelve of these stars will be identified in the following as having statistically significant IR excess. Excluding these stars with excesses and those with signal-to-noise ratio (S/N) < 3 , the average ratio of MIPS flux to predicted photosphere is $|F_{\text{MIPS}}/F_{*}-70\mu\text{m}| = 1.02 \pm 0.05$, consistent with the overall calibration.

The dispersion in the 70 μm data is $\sim 40\%$ (excluding the stars with excesses), consid-

erably higher than that in the 24 μm data. An analysis of the noise levels in each individual field is required to assess whether the IR excesses are statistically significant. Many contributions to the overall error budget must be considered including those arising from stellar photosphere modeling, instrument calibration, sky background variation, and photon detector noise. At 70 μm , the calibration uncertainty and the background noise within each image are considerably larger than at 24 μm . On top of an assumed calibration uncertainty of 15%, we directly measure the standard deviation of the background flux when each field is convolved with our chosen aperture size. This background noise, which ranges from ~ 2 to 20 mJy with a median of 3.7 mJy, is due primarily to extragalactic source confusion and cirrus contamination, rather than photon noise, and hence cannot be greatly reduced by additional integration time (for a more detailed analysis of the 70 μm noise levels, see Bryden et al. 2006a). Based on this measured background noise, we determine the S/N for each star, as listed in Table 2. Despite the high level of noise in some fields due to cirrus contamination and/or background galaxies, 72 out of the 87 stars in our sample with 70 μm data are detected with signal-to-noise ratio greater than 3. The median S/N for all of our target stars is 6.6, excluding the sources identified as having excess emission (which have a median S/N of over 20).

Adding both background noise and calibration error together gives us a total noise estimate for each 70 μm target. In Table 2 we list these noise levels, along with the measured and the photospheric fluxes, for each observed star. We use these noise estimates to calculate χ_{70} which corresponds to the $n - \sigma$ significance of any deviation from the expected level of photospheric emission:

$$\chi_{70} \equiv \frac{F_{70} - F_{\star}}{\sigma_{70}} \quad (2)$$

where F_{70} is the measured flux, F_{\star} is the expected stellar flux, and σ_{70} is the noise level, all at 70 μm . Based on this criterion, we find that 12 out of 88 stars have a $3-\sigma$ or greater excess at 70 μm : HD 25998, HD 38858, HD 40136, HD 48682, HD 90089, HD 105211, HD 109085, HD 139664, HD 158633, HD 199260, HD 219482, and HD 219623. In a sample of 88 stars there should be fewer than 1 star with a spurious excess on purely statistical grounds. Although cirrus or extragalactic confusion could produce spurious excesses, careful examination of each of the 70 μm images suggests that

this is unlikely in the vast majority of cases. For example, the 70 μm emission is well centered on the 24 μm positions, typically within $\sim 1''$. A number of weak excesses could have escaped detection under these criteria. Observations at higher sensitivity or at higher spatial resolution will be needed to identify these. The detection rate of 70 μm excess within this sample is $14 \pm 4\%$; combined with the sample of Bryden et al. (2006a), this gives an overall detection rate of $13 \pm 3\%$ for cool stars.

Four of these stars have been previously identified as having excess emission: HD 40136 ($=\eta$ Lep; Aumann 1988; Mannings & Barlow 1998), HD 48682 ($=\psi$ 5 Aur; Aumann & Probst 1991; Sheret et al. 2004), HD 109085 ($=\eta$ Crv; Aumann 1988; Wyatt et al. 2005), and HD 139664 ($=$ g Lup; Walker & Wolstencroft 1988; Habing et al. 1996; Kalas et al. 2006). The eight newly discovered IR-excess stars mostly have $70\ \mu\text{m}$ fluxes less than 100 mJy, too dim to have been detected by IRAS. The notable exception is HD 105211 which has a very strong $70\ \mu\text{m}$ flux (~ 500 mJy), but lies near a bright infrared source (CL Cru); with a separation of $2.4'$, this source is easily resolved in the MIPS image (Figure 7), but still contaminates the large IRAS beam. For the stars without any significant excess emission, $3\text{-}\sigma$ upper limits on possible excess flux typically range from 0.2 to 1.0 times the stellar flux, with a median of upper limit of $0.6 F_\star$.

Although the telescope resolution at $70\ \mu\text{m}$ is relatively poor (FWHM of $\sim 17''$), several of these sources appear to be slightly extended in the MIPS images (marked with superscript f in Table 2). As discussed in a separate paper (Bryden et al. 2006b), examination of the images of these marginally resolved sources do not indicate contamination by background objects, e.g. cirrus or galaxies, but rather that the objects possess to be truly extended disks. For one of the five Spitzer-resolved disks, HD 139664, a Hubble Space Telescope image shows the same orientation of the disk in the visible as in the infrared (Kalas et al. 2006). At distances of 10-20 pc, the resolved disks have apparent radii of 100's of AU. As discussed below, maintaining a temperature of ~ 50 K at these distances (warm enough to emit strongly at $70\ \mu\text{m}$), requires relatively small grains with low emissivities.

4. Properties of the Detected Dust

Beyond our initial goal of detecting IR excesses, we are interested in determining the properties of the dust in each system - its temperature, luminosity, mass, size distribution, composition, orbital location, etc. For the 12 stars with significant IR excess, Table 4 lists the excess $70\ \mu\text{m}$ emission and measurements of or limits to the $24\ \mu\text{m}$ excess. Seven of the 12 excess sources have an excess measured only at one wavelength ($70\ \mu\text{m}$), restricting our ability to place limits on key quantities. The observed flux can be translated into the total dust disk luminosity relative to its parent star only when some assumption is made for the dust temperature (e.g. Beichman et al. 2005b; Bryden et al. 2006a). The minimum disk luminosity as a function of $70\ \mu\text{m}$ dust flux density is obtained by setting the emission peak at $70\ \mu\text{m}$ (or, equivalently, setting $T_{\text{dust}} = 52.5$ K):

$$\frac{L_{\text{dust}}}{L_\star}(\text{minimum}) = 10^{-5} \left(\frac{5600\ \text{K}}{T_\star} \right)^3 \frac{F_\nu(70\ \mu\text{m}, \text{dust})}{F_\nu(70\ \mu\text{m}, \star)} \quad (3)$$

Based on this equation, a minimum $L_{\text{dust}}/L_{\star}$ is calculated for each of our target stars identified as having an IR excess at only $70 \mu\text{m}$ (Table 4). For the other IR-excess stars, we also have at least a rough ($2\text{-}\sigma$) detection of the $24 \mu\text{m}$ excess, as discussed in the previous section. With two wavelengths of excess measurement, the dust emission can be fit with a representative dust temperature, otherwise only upper limits can be obtained (Table 4; also see Figure 11 below). Figure 8 shows a spectral energy distribution (SED) for two of these stars, HD 219482 and HD 40316, fit with temperatures of 170 and 80 K respectively. In the cases with a fit dust temperature, Table 4 lists the ratio of the integral under the stellar (T_{\star}) and dust (T_{dust}) blackbodies as a proper, rather than minimum, estimate of $L_{\text{dust}}/L_{\star}$:

$$\frac{L_{\text{dust}}}{L_{\star}} = \left(\frac{T_{\text{dust}}}{T_{\star}} \right)^4 \left(\frac{e^{x_{\text{dust}}} - 1}{e^{x_{\star}} - 1} \right) \frac{F_{\nu}(70 \mu\text{m}, \text{dust})}{F_{\nu}(70 \mu\text{m}, \star)} \quad (4)$$

where $x \equiv h\nu/kT = 205.7 \text{ K}/T$ at $70 \mu\text{m}$.

For each of the stars with excess emission (plus those from Bryden et al. (2006a), Figure 9 shows the total dust area and radial location of the emitting material. Despite the expectation that only large grains should be seen around mature systems due to loss mechanisms such as Poynting-Robertson drag and radiation pressure, small grains must be considered as a serious possibility given their presence in a mature star like HD 69830 (Beichman et al. 2006) and because of the large extent of at least some the dust disks. Thus, the orbital location of the emitting material can only be calculated if some assumption is made for the dust’s emissivity; small grains are less efficient at emitting infrared radiation, resulting in a higher temperature for a given orbital radius. For a given dust temperature, the orbital radius decreases with emissivity as $\epsilon^{-0.5}$. As such, for each calculated dust temperature or upper limit in Table 4, two locations are plotted - the location if the emitting material is large blackbodies (lower axis) and the location if it is small grains with emissivity = 0.01 (upper axis).

The dust area and mass have a similar ambiguity based on the unknown dust size/emission properties. The dust area in Figure 9 (left axis) is calculated under the assumption of blackbody grains (unity emissivity); a lower emissivity would increase the dust area in direct proportion to ϵ . Lastly, the dust mass (right axis) is based on an assumed typical grain size of $10 \mu\text{m}$. An unconstrained amount of mass is contained in the larger parent bodies whose collisions produce the emitting dust.

For stars with no detected emission, $3\text{-}\sigma$ upper bounds on the $70 \mu\text{m}$ fluxes lead to upper limits on $L_{\text{dust}}/L_{\star}$ as low as a few times 10^{-6} , assuming a dust temperature of $\sim 50 \text{ K}$ (Table 2). Although we cannot rule out cold dust at $\gtrsim 100 \text{ AU}$, we are placing constraints on dust at Kuiper Belt distances to $\sim 10\text{-}100$ times the level of dust in our solar system. The constraint on asteroid belt-type dust is less stringent, $\sim 100\text{-}1000$ times our zodiacal

emission.

4.1. Comparison with Sub-mm Observations

The dust properties can be further constrained with sub-mm flux measurements. When available, longer wavelength data can help place lower limits on dust temperature, upper limits on the dust luminosity, and, with some assumption on the grain emissivity, outer limits on the disk extent. For most of our stars with IR excess, large amounts of cold dust emitting at longer wavelengths cannot be ruled out, but three of the 70 μm excess stars have been observed at 450 and 850 μm with JCMT/SCUBA, with two detections (HD 48682 and HD 109085) and one upper limit (HD 139664; Sheret et al. 2004). Combining their sub-mm data with the infrared fluxes from IRAS, Sheret et al. (2004) modeled the SEDs for these stars, obtaining dust temperatures of 99 and 85 K for HD 48682 and HD 109085, respectively.

4.2. Comparison with Visible Observations

A nearly edge-on disk around HD 139664 has recently been detected at visible wavelengths using the Hubble Space Telescope (HST) (Kalas et al. 2006). The HST image of the disk shows a well defined inner edge around 83 AU and an outer edge that extends out to about 109 AU. If the dust associated with the 70 μm emission is located in this ring, then a very large surface area of 10 μm grains would be required for the IR emission, since dust at this distance would have an equilibrium temperature of 30-35 K using a standard radial power law for grain temperature (Beichman et al. 2006). Smaller, 0.25 μm grains, on the other hand, give temperatures of 69 and 77 K at the ring boundaries (cf. our 3-sigma upper limit of 78 K; Table 4). Using a simple relationship for dust mass, $M_{dust} = \frac{4}{3}\rho a_{grain} \frac{D^2 F_{\nu}(dust)}{Q_{abs} B_{\nu}(T_{dust})}$, and standard silicate absorption efficiencies, Q_{abs} (Draine & Lee 1984; Beichman et al. 2006), yields a mass of $2.4 \times 10^{-3} M_{\oplus}$ in large grains or $1.6 \times 10^{-4} M_{\oplus}$ in small grains, where we have taken a grain density of $\rho=3.3 \text{ gm cm}^{-3}$ and a distance, $D = 17.5 \text{ pc}$, for this star.

The radiative blowout size for grains around an F5 star is approximately 1 μm (§V.B.1 in Backman & Paresce (1993); Burns et al. (1979)). In contrast to the spherical distribution of small grains seen toward Vega (Su et al. 2005) which is probably due to a recent catastrophic event, small grains should be quickly ejected from the presumably stable ring system of HD 139664. IRS spectroscopy and/or millimeter spectroscopy would help distinguish between the large and small grain models.

5. Correlation of Excess with System Parameters

To understand the origin and evolution of infrared excess, we now consider the properties of the sample stars and how they correlate with excess detection. Specifically, we examine the correlation with three variables: metallicity, age, and spectral type. These parameters are listed for each star in Table 1. Where appropriate we merge the present sample with that of Bryden et al. (2006a) to improve the significance of any statistical conclusions.

5.1. Metallicity

Table 1 lists the metallicity information obtained from the literature for each of our target stars (number of independent $[\text{Fe}/\text{H}]$ estimates, their average, and their r.m.s. scatter). Figure 3 shows a histogram of these metallicity values, the majority of which range between -0.4 to $+0.1$ dex with a mean value of somewhat below solar. The stars with IR excess are identified with vertical arrows with the length of each arrow proportional to the strength of $70\ \mu\text{m}$ excess. We find no correlation between metallicity and IR excess. The average $[\text{Fe}/\text{H}]$ is -0.15 ± 0.03 for all the observed stars and -0.17 ± 0.04 for the stars with excess - an insignificant difference.

These data are combined with Bryden et al. (2006a) sample to show the fractional incidence of disks as a function of $[\text{Fe}/\text{H}]$ (Figure 12). A χ^2 test shows that the distribution of disks in our three metallicity bins with significant number of stars ($-0.75 < [\text{Fe}/\text{H}] < 0.0$) is indistinguishable from flat. The lack of correlation between IR excess and metallicity is in sharp contrast with the well known correlation between extrasolar gas giant planets and host star metallicity (Gonzalez 1997; Santos et al. 2001). In particular, Fischer & Valenti (2005) find that the probability of harboring a radial-velocity detected planet increases as the square of the metallicity (Figure 12). Although one might suspect giant planets and debris disks to be related, a similarly strong correlation between dust and metallicity can be confidently ruled out. A χ^2 comparison between the disk and planet distributions in same 3 $[\text{Fe}/\text{H}]$ bins suggest that there is only a 0.3% probability of these being drawn from the same distribution.

The lack of correlation is further confirmed via Monte Carlo simulations. Again using our dataset combined with that of Bryden et al. (2006a) (giving a total of 19 excess stars out of 151 observed), the correlation coefficient, r , is calculated for 10,000 random samples of stars. The histogram of the resultant r values is shown in Figure 13 under two different assumptions. In one case, the stars with excess are chosen randomly (left histogram centered on $r=0$); in the other, the stars are chosen with weighting proportional to their metallicity

squared (right histogram with average $r=0.33$). The correlation coefficient observed within our data (vertical arrow) is inconsistent with the strong metallicity dependence observed within planet-bearing stars.

This lack of correlation may reflect the different formation histories of giant planets and debris disks. The accretion of gas onto a giant planet requires a large solid core to form first, favoring a higher metallicity disk, whereas dust emission indicates the presence of smaller planetesimals that might be able to form in all disk environments. Another explanation may be that debris disks in high metallicity systems initially contain more material, but that over time all disks grind down toward similar masses (e.g. Dominik & Decin 2003). In this case, the detection of strong IR emission is a reflection of a recent stochastic collision, rather than the disk’s initial conditions (see Bryden et al. (2006a) for further discussion).

5.2. Age

Collisions in a debris disk continually grind down the larger planetesimals, while the smallest dust can be removed by Poynting-Robertson drag and radiation pressure. One would assume that the overall disk mass must decline with time and, as expected, a correlation between stellar age and IR excess is observed, with debris disks more commonly identified around younger stars. While studies concentrating on stars younger than 1 Gyr find a strong trend (Spangler et al. 2001; Rieke et al. 2005), among nearby solar-type field stars the correlation is relatively weak (Bryden et al. 2006a). In both cases, the evolution of the dust does not appear to be a steady decline. Observations of A stars find an overall decline in the average amount of $24 \mu\text{m}$ excess emission on a ~ 150 Myr time scale, but the large variations on top of this trend suggest that sporadic collisional events are able to dramatically increase the amount of dust even at late stages in the disk’s evolution (Rieke et al. 2005). As a result of these collisions, even old stars can have strong IR emission (Habing et al. 2001; Decin et al. 2000; Bryden et al. 2006a).

Figure 2 shows the resultant histogram of stellar ages. The ages for our main sequence stars are difficult to determine, with uncertainties in many cases of at least a factor of two. Where possible, we use ages based on Ca II H&K line emission from the large compilation of Wright et al. (2004). Otherwise an average of values found in the literature is used. If the star was inferred to be young due to kinematic properties (Montes et al. 2001), we adopted that age. Table 1 lists the age data for each star. Although our target selection criteria do not explicitly discriminate based on stellar age, young stars (ages less than 1 Gyr) are not well represented in our sample due to their infrequent occurrence within ~ 25 pc of the Sun.

As in our earlier survey of nearby main-sequence stars (Bryden et al. 2006a), the stars with excess in this survey (marked with arrows in Figure 2) have a weak but noticeable correlation with stellar age. No stars older than 7 Gyr have a significant amount of excess emission. The average age of stars with IR excess is 4.0 ± 0.6 Gyr, compared to 5.6 ± 0.4 Gyr for the sample as a whole. As discussed in the next section, these trends are present in the combination of this sample with the Bryden et al. (2006a) data.

5.3. Spectral Type

Observations of the general characteristics of debris disk as a function of spectral type are potentially a powerful tool for understanding the physical mechanisms responsible for the evolution of debris disks. The disk properties should be directly related to the stellar mass and luminosity in several ways. The mass of the protostellar disk from which the debris formed, for example, probably depends on the parent star’s mass, as does its dynamical time scale. The stellar luminosity, though, is undoubtedly more important for debris disk characteristics, exerting a strong influence on the typical particle size ($r_{\text{blowout}} \propto L_{\star}$) as well as its temperature ($T_{\text{dust}} \propto L_{\star}^{0.2-0.25}$). There are also observational biases linked to the brightness of the star, with cool dust seemingly easier to distinguish around hotter stars.

The minimum $L_{\text{dust}}/L_{\star}$ based on the $70 \mu\text{m}$ flux, for example, is strongly dependent of stellar temperature (in eq. [3], detectable $L_{\text{dust}}/L_{\star}$ is proportional to T_{\star}^{-3}). Hotter stars emit a lower fraction of their luminosity at infrared wavelengths, allowing for better contrast at those wavelengths. But while equation (3) is an observationally well-defined quantity, it contains no knowledge of the underlying disk physics. Naively, it appears to dictate a strong relationship between detectability and spectral type, i.e. it is easier to detect dust around hotter stars, but this may be misleading. For lack of any other information, the equation assumes that the dust emission peaks at $70 \mu\text{m}$, thereby measuring the minimum $L_{\text{dust}}/L_{\star}$. This assumed SED shape corresponds to a fixed dust temperature of ~ 50 K for all disks. One can instead consider disk models with a more physically motivated dependence on spectral type. Instead of assuming a constant dust temperature, Habing et al. (2001), for example, assume the same dust *location* for all disks; in their models, the dust resides at 50 AU independent of spectral type. In this case, dust temperature decreases with T_{\star} . In contrast with a simple reading of equation (3), the Habing et al. models have $L_{\text{dust}}/L_{\star}$ more or less directly proportional to $F_{\text{dust}}/F_{\star}$ for stars of type G and earlier. As in equation (3), lower stellar temperature makes it more difficult to detect dust emission relative to the stellar photosphere, but in Habing et al.’s models this difficulty is offset by a lower dust temperature for cooler stars, increasing the dust’s $70 \mu\text{m}$ emission.

In Figure 1, the spectral types with IR excess stars are flagged with vertical arrows. A clear trend is readily apparent, with excess more frequently detected around earlier type stars. The detection rate drops from nearly 30% for the earliest type stars down to 0% for M stars. In fact, no stars with spectral type later than K0 are found to have excess emission (a sample of 23 stars without excess). This is consistent with previous survey results that considered only part of the spectral range covered here. Our survey of F5-K5 stars (Bryden et al. 2006a) found a detection rate of 13% within this limited spectral range, while a sample of ~ 30 images of nearby M stars yielded none with IR excess at $70 \mu\text{m}$ (Gautier et al. 2006).

A possible interpretation of the trend with spectral type is that it simply reflects the known correlation with stellar age. Earlier spectral type stars tend to be younger. Figure 10 combines information on spectral type and age into a single plot for stars in this survey and those of Bryden et al. (2006a). The trends previously identified are apparent - an upper limit to the ages of stars with excesses (filled symbols) of about 6 Gyr and a tendency for earlier type stars to have excess more frequently than later types. While the earliest type stars (F0-F3) are clearly younger on average, there is no clear evidence within the bulk of the sample that higher mass stars have more frequent excess because of they have younger ages. The formal correlation of excess with spectral type is even stronger than the correlation with age (correlation coefficients are -0.20 ± 0.08 . and -0.15 ± 0.08 for spectral type and age respectively), further suggesting that spectral type is an independent indicator for IR excess. Unfortunately many of the latest type stars lack reliable age indicators, making it difficult to make any stronger conclusions.

5.3.1. Comparison with Early Type Stars

The detection rate of $70 \mu\text{m}$ excess around A stars is $33 \pm 4\%$ (Su et al. 2006), more than twice that for the stars considered in this paper ($13 \pm 3\%$). However, the A star and FGK star samples differ in both mass and age. We first consider the possibility that the different detection rates simply reflect an age evolution, rather than a spectral type dependence. For example, the youngest FGK stars have a detection rate somewhat higher than that within the sample as a whole: considering only systems with ages of 0.1-1 Gyr (and including the stars from Bryden et al. (2006a)), 5 out of 19 young FGK stars have excess $70 \mu\text{m}$ emission ($= 26 \pm 12\%$). Similarly, the $70 \mu\text{m}$ excess frequency among the A stars drops with stellar age down to just $21 \pm 6\%$ for A stars 0.3 - 1 Gyr old (Su et al. 2006). It is important to note, however, that many of the Su et al. (2006) observations are less sensitive than those presented here, relative to the stellar photosphere. Thus, their A star detection rate should

be regarded as a lower limit. Although the FGK and A star samples have stellar age as the most important correlating factor for IR excess, we cannot rule out a weaker but still important dependence of IR excess on some factor related to stellar mass such as luminosity or disk mass.

5.3.2. Comparison with Late Type Stars

Combining the observations presented here with those of Bryden et al. (2006a) and Gautier et al. (2006), we have a total sample of 61 K1-M6 stars with no evidence of excess emission at $70\ \mu\text{m}$. Even considering only those stars whose photospheres are detected at $70\ \mu\text{m}$ with $S/N > 3$ (42 of the 61 stars), this lack of excess detections is $>3\text{-}\sigma$ inconsistent with the $\sim 15\%$ detection rate around F and G type stars. As implied by Eqn (3), the contrast of dust relative to photosphere is, however, poorer for cooler stars which emit more of their energy in the infrared than hotter stars. The average upper limit to $L_{\text{dust}}/L_{\star}$ for the 16 stars K1 or later with detected photospheres but no excesses in the SIM/TPF sample ($S/N(70\mu\text{m}) > 3$ and $\chi_{70} < 3$) is $L_{\text{dust}}/L_{\star} < 9 \times 10^{-6}$ compared with the average upper limit for 51 hotter stars with detected photospheres but no excesses, $L_{\text{dust}}/L_{\star} < 4 \times 10^{-6}$. Thus, one explanation for the lack of excesses around later-type stars is simply that the effective observational limits are a factor of two higher for the cooler stars. While observational selection effects make detection of IR excess around late type stars more difficult, the strength of this trend suggests that other explanations are needed.

Another ambiguity in interpreting the correlation of excess with spectral type results from our limited knowledge of the location of the dust. If dust around later type stars is very distant from its central star, it will be too cool for detection at $70\ \mu\text{m}$. Figure 11 shows how the dust temperature varies as a function of spectral type for stars with excess from both this sample and from Bryden et al. (2006a). We can only derive a dust temperature in the limited number of cases where we have a measured excess at both 24 and $70\ \mu\text{m}$ (*solid points*). Otherwise, only upper limits can be obtained (Table 4). For unresolved disk observations, the dust location cannot be determined without some knowledge of the underlying dust emission properties. Smaller dust with low emissivity can be just as hot as larger grains closer to the central star. Lines of constant orbital radius are shown in Figure 11 under the assumption of either large blackbody grains ($\epsilon = 1$) or of small grains with emissivity = 0.01. Although the observed temperatures range from 80 to 170 K, they are all more or less consistent with emission from similar orbital locations: 10 AU for $\epsilon = 1$ or 100 AU for $\epsilon = 0.01$. By implication, one would expect that dust around later K stars might have typical temperatures of ~ 50 K, ideal for detection at $70\ \mu\text{m}$, though none were

detected.

Additional information on the location of the dust comes from IRS observations of F, G, and K stars with excesses (Beichman et al. 2006) which reveal that in almost all cases the inner boundary of the emitting region occurs at or interior to 10 AU. A theoretical basis for this preferred location of a radial distance of a few AU comes from the suggestion that the water-ice sublimation distance, or the “snowline” where the temperature falls below 170 K, should mark the onset of the region of giant planet formation and its remnants in the Kuiper Belt (Hayashi 1981; Sasselov & Lecar 2000; Garaud & Lin 2006). Since the location of the snowline varies with stellar luminosity ($\propto L^{0.25}$), there is no reason to expect a more distant, hidden reservoir of material unsampled by our observations around cooler stars. It is, of course, important to verify this expectation with observations at longer wavelengths such as MIPS 160 μm and in the sub-millimeter. Within the Gautier et al. (2006) sample, for example, none of the 20 M stars examined at 160 μm show any excess emission, providing limits on $L_{\text{dust}}/L_{\star}$ of 10^{-5} - 10^{-3} for material at ~ 50 AU.

If the lack of debris disks around cool stars is real, then the dearth of material might reflect different formation mechanisms and evolutionary history for the belts of planetesimals around low mass stars. Dust-producing collisions within these belts, for example, may require planetesimal stirring by larger, gas-giant planets, whose frequency is thought to be lower for late-type stars (Laughlin et al. 2004). Alternately, the lack of IR excess might instead indicate a change in the physics of the smallest orbiting bodies as later type stars are considered, such as the increased relative importance of stellar winds in clearing dust from the system (Plavchan et al. 2005).

6. Applicability to TPF

The detection of other terrestrial planets is a long term goal for the astronomical community (McKee & Taylor 2001). NASA has spent considerable funds over the past decade on technology development and mission studies for a Terrestrial Planet Finder (TPF). One of the key astro-engineering issues revealed by those studies is the level of dust emission associated with target stars since exo-zodiacal emission is potentially an important source of photon shot noise (Beichman et al. 1999). Thus, in addition to scientific interest, the incidence and distribution of material in the habitable zones, i.e. where planets might have surface temperatures consistent with the presence of liquid water (Kasting et al. 1993), of nearby stars is of considerable technical importance.

6.1. Effect of Exo-Zodiacal Dust on Planet Finding

As discussed in Appendix A, dust emission at the level of 10-20 times that of our own zodiacal cloud can impede planet searches (Figure 15) due to increased photon shot noise for either a coronagraph or an interferometer. Since this level is roughly 50-100 times less than that presently detectable with *Spitzer*, we can rule out only those stars with the most extreme zodiacal disks. Thus, HD 109085 and HD 69830 (Beichman et al. 2005a) are unsuitable targets with strong excess shortward of $24 \mu\text{m}$. However, the remaining stars in this sample and other samples pass the initial screening by having $24 \mu\text{m}$ excesses, if any, less than $L_{\text{dust}}/L_{\star} \simeq 10^{-4}$, corresponding to upper limits on $\mu_{EZ} \sim 500$ (Bryden et al. 2006a). Beyond these photometric constraints, IRS spectroscopy can push upper limits to factors of 2-3 lower than MIPS alone and can also identify stars with small grain emission at $10 \mu\text{m}$ (Beichman et al. 2006).

In a few cases listed in Table 6 we can use the blackbodies fitted to the emission from the 5 stars with data at both

24 and $70 \mu\text{m}$ (Table 4) to extrapolate the emission from this “Kuiper Belt” dust to the prime TPF-I wavelength of $10 \mu\text{m}$. The extrapolated emission is also given in units of $L_{\text{dust}}/L_{\star}$ for material emitting at $10 \mu\text{m}$ (cf. eq. [3] and eq. [2] of Beichman et al. (2006)) relative to the solar system value of 10^{-7} (Backman & Paresce 1993). Emission from any of this material located within the primary beam of the TPF-I telescopes ($r < 5$ AU for a star at 10 pc observed with 3 m apertures) would be a noise source as described in the Appendix. However, this population of “cool” or “lukewarm” grains would not be located within a TPF-C pixel centered on the ~ 1 AU habitable zone and would not be a noise source at visible wavelengths.

Unfortunately, however, the present observations cannot rule out an additional population of hotter grains located closer to the star which would either emit at $10 \mu\text{m}$ or scatter in the visible. IRS observations in the 8-14 μm region reach levels of just 1,000 times the zodiacal level (Beichman et al. 2006). It will take observations with nulling Interferometers such as the Keck and Large Binocular Telescope Interferometers which can spatially suppress the stellar component to measure directly the exo-zodiacal emission in the habitable zone at levels that could cause S/N or confusion problems for TPF.

There is some cause for optimism, however. The “luminosity function” of disks inferred from a variety of *Spitzer* samples (Bryden et al. 2006a), the rarity of extreme “hot” zodiacal disks in the sample reported here and in other *Spitzer* papers (Bryden et al. 2006a; Beichman et al. 2006), and the apparent decline in the number of stars with excesses as a function of age (Fig. 2) are all encouraging signs that the relatively clean example of our

solar system may be the norm rather than the exception. The ring-like structures seen in a number of resolved Spitzer disks, e.g. Fomalhaut (Stapelfeldt et al. 2004) and ϵ Eri (Backman et al., in preparation) as well as in HST images (Kalas et al. 2005, 2006) suggest that although the regions interior to the rings may not be completely empty due to a variety of mechanisms capable of transporting material inward from the outer disk (comets, PR drag, interactions with planets, etc.; Holmes et al. 2002), these interior regions may have a quite low total optical depth, perhaps as low as the $\sim 20\%$ contribution inferred for material from Kuiper Belt material to the total amount seen at 1 AU in our solar system (Landgraf et al. 2002; Dermott & Kehoe 2004; Moro-Martín & Malhotra 2005).

7. Summary

We have searched for circumstellar dust around a sample of 88 F-M stars, by means of photometric measurements at $24\ \mu\text{m}$ and $70\ \mu\text{m}$. We detected all the stars at $24\ \mu\text{m}$ with high S/N and more than 80% of the stars at $70\ \mu\text{m}$ with $S/N > 3$. Uncertainties in the *Spitzer* calibration and in the extrapolation of stellar photospheres to far-IR wavelengths limit our ability to detect IR excesses with $3\text{-}\sigma$ confidence to $\sim 20\%$ and $\sim 50\%$ of the photospheric levels at 24 and $70\ \mu\text{m}$, respectively.

At these levels we have detected 12 of 88 objects with significant $70\ \mu\text{m}$ excesses. Combined with an earlier study (Bryden et al. 2006a), we find an overall detection rate of $13 \pm 3\%$ for mature cool stars. Beyond the single previously known $24\ \mu\text{m}$ excess within our sample, we detect two objects with $70\ \mu\text{m}$ excesses and definite but weak $24\ \mu\text{m}$ emission. Another two stars with $70\ \mu\text{m}$ excesses have $2 - \sigma$ hints of $24\ \mu\text{m}$ excesses. These results build on the finding of Beichman et al. (2006) that in many cases, objects with $70\ \mu\text{m}$ emission also had IRS spectra rising longward of $25\ \mu\text{m}$ to meet the $70\ \mu\text{m}$ excess. These objects are all consistent with a disk architecture similar to our Kuiper Belt that is concentrated outside 5-10 AU. In this context we note that a number of the $70\ \mu\text{m}$ sources are slightly, but significantly extended at $70\ \mu\text{m}$. The detailed discussion of these objects is deferred to a subsequent paper (Bryden et al. 2006b). The IR emission in these systems is different from the exceptional object HD 69830, which shows a disk architecture much more consistent with a massive asteroid belt (Beichman et al. 2005a).

Cross-correlating the detections of IR excess with stellar parameters we find no significant correlations in the incidence of excesses metallicity, but do find weak correlations with both stellar age and spectral type. The lack of correlation with metallicity contrasts with the known correlation between planet detections and stellar metallicity, and the expectation that higher metal content might result in a greater number of dust-producing planetesimals.

One significant finding is that the incidence of debris disks among mature stars is markedly lower for spectral types later than K0 than for earlier spectral types. Combining data from this survey, the Bryden et al. (2006a) F5-K5 survey, and the Gautier et al. (2006) M star survey suggests an incidence of disks of $15\pm 3\%$ for F0-K0 stars and $0\pm 4\%$ for stars with types K2-M3. This lack of disks around later spectral types may be due to selection effects, lower initial disk mass, or different rates of dust creation or destruction.

The disks that we are detecting have typical $70\ \mu\text{m}$ luminosities around 100 times that of the Kuiper Belt. If they also have inner asteroid belts 100 times brighter than our own, however, we would still not be able to detect this warm inner dust. The observed $70\ \mu\text{m}$ excess systems could all be scaled-up replicas of the solar system’s dust disk architecture, differing only in overall magnitude. These systems could have planets, asteroids and Kuiper Belt Objects as in our own system, but simply with a temporarily greater amount of dust due to a recent collisional event. Further observations of the warmer inner dust are necessary to address this possibility. *Spitzer*/IRS is particularly promising in this regard (Beichman et al. 2006) and is being pursued as part of a follow-up effort for some of the stars in this program.

This publication makes use of data products from the Two-Micron All Sky Survey (2MASS), as well as from IPAC, SIMBAD, VIZIER, and the ROE Debris Disks Database website. We gratefully acknowledge the assistance of John Carpenter in reducing the IRAC data reported in this paper and we thank Angelle Tanner and Kate Su for helpful discussions. The *Spitzer Space Telescope* is operated by the Jet Propulsion Laboratory, California Institute of Technology, under NASA contract 1407. Development of MIPS was funded by NASA through the Jet Propulsion Laboratory, subcontract 960785. Some of the research described in this publication was carried out at the Jet Propulsion Laboratory, California Institute of Technology, under a contract with the National Aeronautics and Space Administration.

A. Noise Due to Exo-Zodiacal Emission

In this section we make order of magnitude estimates of the impact of photon noise from exo-zodiacal emission on both visible light and mid-IR instruments (TPF-Coronagraph and TPF-Interferometer, respectively) designed to find neighboring planets. A detailed noise analysis of planet finding telescopes is beyond the scope of this paper and the reader is referred to other articles for more details (Beichman & Velusamy 1999; Brown 2005).

A.1. TPF-I, The Infrared Interferometer

The use of a nulling interferometer to reject starlight and thereby reveal an orbiting planet dates to an article by Bracewell (1978) and has been further investigated through studies of more sophisticated configurations (Angel & Woolf 1997; Lay et al. 2005). For a cryogenic system operating in an orbit near 1 AU, the three dominant noise sources are (Beichman & Velusamy 1999, Table 5): the stellar light that leaks past the interferometric null because of the finite diameter of the star, $S_{*,Leak}$; emission from the local zodiacal dust, S_{LZ} ; and emission from the exo-zodiacal dust in the target star system that leaks past the interferometer, $S_{EZ,Leak}$ (see Figure 14). At short wavelengths ($< 8 \mu\text{m}$), the stellar leak may dominate all other noise sources; longward of $20 \mu\text{m}$ emission from a 35 K telescope will become important; and at all wavelengths various systematic instrumental effects will be important. But over a broad range of wavelengths, the balance between $S_{*,Leak}$, S_{LZ} , $S_{EZ,Leak}$ controls the fundamental noise floor. Detector read noise and dark current can be ignored for broad band detection.

In the background limit considered here, the total noise is given by the square root of the sum of all the individual photon fluxes reaching the detector. Rather than evaluate the absolute signal-to-noise ratio, S/N, we consider here the ratio of the S/N in the presence of exo-zodiacal emission, $\text{SNR}(EZ)$, to the S/N in the absence of such emission, $\text{SNR}(0)$:

$$\left. \frac{\text{SNR}(EZ)}{\text{SNR}(0)} \right|_{IR} = \frac{\sqrt{S_{*,Leak} + S_{LZ}}}{\sqrt{S_{*,Leak} + S_{LZ} + S_{EZ,Leak}}} = \frac{\sqrt{1 + \frac{S_{*,Leak}}{S_{LZ}}}}{\sqrt{1 + \frac{S_{*,Leak}}{S_{LZ}} + \frac{S_{EZ,Leak}}{S_{LZ}}}} \quad (\text{A1})$$

In the above, $S_{*,Leak}$ depends on the nulling configuration, the wavelength of operation and the angular size of the star. Null depths of 10^{-5} to 10^{-6} have been demonstrated in the laboratory (Martin et al. 2003) and for the purposes of this illustration, it suffices to take $S_{*,Leak} = 10^{-5}F_*$. The emission from the local zodiacal cloud, S_{LZ} , is very complex in detail (Kelsall et al. 1998), but can be parameterized for our purposes as follows, $S_{LZ} = \tau_{LZ}B_\nu(255 \text{ K})\Omega_{tel}$ where B_ν is the Planck function, τ_{LZ} is the vertical optical depth looking out from the mid-ecliptic plane at 1 AU, and Ω_{tel} is the diffraction limited solid angle of an individual telescope in the interferometer. A typical value of the zodiacal cloud brightness toward the ecliptic pole from our mid-plane location is 12 MJy sr^{-1} at $12 \mu\text{m}$ (Kelsall et al. 1998).

In the absence of more detailed information, the vertical optical depth of the exo-zodiacal dust in any system can be parameterized as a factor, μ_{EZ} , times the Solar System's zodiacal dust. The emission from exo-zodiacal dust is then $S_{EZ}(r) = 2\mu_{EZ}\tau_{LZ}(r)B_\nu(T(r))\Omega_{tel}$, where

the factor of two accounts for the fact that in the exo-zodiacal case we are looking through the entire cloud and not from the vantage of the mid-plane as we do the local cloud. By analogy with the local zodiacal cloud (Backman 1998) the vertical optical depth is assumed to fall off radially as $\tau_{LZ}(r) = \tau_{LZ,1AU} r_{AU}^{-0.3}$. We also take $T(r) = T_0 r_{AU}^\beta$ as the equilibrium temperature for grains heated by stellar radiation and emitting in the infrared. Typical 1 AU values of (T_0, β) for large and small silicate grains are (255 K, -0.5) and (362 K, -0.4), respectively (Draine & Lee 1984; Backman & Paresce 1993; Beichman et al. 2006). The large and small grain brightness distributions are normalized to yield the same value at 1 AU.

The effect of exo-zodiacal emission is modulated by the fringe pattern of the interferometer which attenuates the bright central portion of the exo-zodiacal disk. To account for this effect we incorporate the fringe pattern of a particular nulling scheme $\zeta(\theta, \phi)$ where θ and ϕ are the radial and azimuthal variables, respectively. In the simplified case of a face-on disk, the signal reaching the detector, $S_{EZ,Leak}$ is then given by the integral of S_{EZ} over the fringe pattern and the telescope solid angle:

$$S_{EZ,Leak}(d) = \int_0^{2\pi} d\phi \int_0^{\theta_{max}} \mu_{EZ} \tau_{LZ}(\theta d) B_\nu(T(\theta d)) \zeta(\theta, \phi) \theta d\theta \quad (A2)$$

for a star at a distance d . We adopt the fringe pattern $\zeta(\theta, \phi)$ for the Dual Chopped Bracewell interferometer (DCB; Lay 2004; Lay et al. 2005) presently under study. Canceling out common factors, the stellar leak term in equation (A1) then becomes

$$\left. \frac{S_{EZ,Leak}(d)}{S_{LZ}} \right|_{IR} = 2\mu_{EZ} \left(e^{\frac{14388}{\lambda T_{LZ}}} - 1 \right) \frac{1}{\Omega_{tel}} \int_0^{2\pi} d\phi \int_0^{\theta_{max}} \frac{\zeta(\theta, \phi) (\theta d)^{-0.3}}{e^{14388/(\lambda T(\theta d))} - 1} \theta d\theta \quad (A3)$$

To evaluate equation (A3), we adopt a diffraction limited beam size of $\theta_{max} = 0.6\lambda/D = 0.5''$ for a $D = 3$ m telescope at $12 \mu\text{m}$. For a solar-type star at $d = 10$ pc, the ratio of the exo-zodiacal contribution to that from the Solar System's own dust (eq. A3) is $0.06 \mu_{EZ}$ or $0.24 \mu_{EZ}$, for large and small grains respectively. Warmer, smaller grains fill more of the beam of the individual telescopes than the cooler, larger (blackbody) grains and thus contribute more noise. With this information in hand, Figure 15 shows the variation of S/N as a function of exo-zodiacal brightness, μ_{EZ} , for two grain sizes. When the exo-zodiacal surface density μ_{EZ} is 10 times that of our solar system, corresponding to a 20-fold brightness increase, the S/N is reduced by a factor of ~ 2 , necessitating an increase in integration time by a factor of ~ 4 to recover the original S/N. It is interesting to note the importance of grain size on this effect; the emission from the large grains is more centrally peaked and thus more effectively attenuated by the nulling interferometer than for the smaller grains which remain warm at quite large distances from the star. Since at least a few hours of integration time is needed to detect an Earth in the presence of a $\mu_{EZ} = 1$ cloud, and days to carry out

a spectroscopic program (Beichman 1998; Lay et al. 2005), it is clear that studying systems with $\mu_{EZ} > 10 - 20$ will be difficult.

A.2. TPF-C, the Visible Light Coronagraph

A similar analysis can be applied to an assessment of the effects of exo-zodiacal emission at visible wavelengths. There are some important differences however. First, the coronagraph takes in only the exo-zodiacal light from the immediate vicinity of the planet, not from the entire exo-zodiacal cloud (Fig. 14, *right side*). Second, the signal from an Earth (S_p), the residual starlight after a 10^{-10} rejection ratio, and the local and exo-zodiacal signals are all more evenly balanced. Detector noise becomes a serious issue at medium spectral resolution (~ 75), but can be ignored in the broadband case. The analog of equation (A1) for the coronagraph becomes:

$$\frac{SNR(EZ)}{SNR(0)} \Big|_{Vis} = \frac{\sqrt{1 + \frac{S_{*,residual}}{S_{LZ}} + \frac{S_p}{S_{LZ}}}}{\sqrt{1 + \frac{S_{*,residual}}{S_{LZ}} + \frac{S_p}{S_{LZ}} + \frac{S_{EZ}}{S_{LZ}}}} \quad (A4)$$

Since the local and exo-zodiacal emission enter the system through exactly the same solid angle, Ω_{tel} , the $\frac{S_{EZ}}{S_{LZ}}$ term simplifies to $2\mu_{EZ}$. For a planet 25 mag fainter than a V=4.5 mag solar twin at 10 pc, and assuming a local zodiacal brightness of 0.1 MJy sr⁻¹ at 0.55 μ m (Table 5; Bernstein et al. 2002), we can evaluate the variation in S/N as a function of μ_{EZ} . Figure 15 shows the decrease in S/N as the exo-zodiacal emission increases in the case of a face-on disk; an edge-on disk will increase the surface brightness and resultant noise. As with the interferometer, the effect of zodiacal emission in the target system is to lower the S/N by a factor of 2~3 at $\mu_{EZ} = 10$.

The *relative* effect of the exo-zodiacal emission is somewhat more pronounced for the TPF-C than for the TPF-I because the interferometer is dominated by the strong *local* zodiacal background until very bright exo-zodiacal levels are observed. The intrinsic background level within the visible-light coronagraph is low (by assumption of an excellent 10^{-10} rejection ratio) so that the exo-zodiacal emission more quickly plays a significant role in setting the system noise.

A more detailed examination of the effects of the exo-zodiacal emission on the detectability of planets using TPF-C and TPF-I would yield absolute, not relative, sensitivity levels including the effects of disk inclination and confusion by structures, e.g. wakes and gaps, within the zodiacal cloud. These questions lie beyond the scope of this paper.

REFERENCES

- Angel, J. R. P. & Woolf, N. J. 1997, *ApJ*, 475, 373
- Aumann, H. H. 1988, *AJ*, 96, 1415
- Aumann, H. H. & Probst, R. G. 1991, *ApJ*, 368, 264
- Backman, D. E. 1998, in *Exozodiacal Dust Workshop*:, 107
- Backman, D. E. & Paresce, F. 1993, in *Protostars and Planets III*, 1253–1304
- Barry, D. C. 1988, *ApJ*, 334, 436
- Beichman, C. A. 1998, in *Proc. SPIE Vol. 3350*, p. 719-723, *Astronomical Interferometry*, Robert D. Reasenberg; Ed., 719–723
- Beichman, C. A., Bryden, G., Gautier, T. N., et al. 2005a, *ApJ*, 626, 1061
- Beichman, C. A., Bryden, G., Rieke, G. H., et al. 2005b, *ApJ*, 622, 1160
- Beichman, C. A., Bryden, G., Stapelfeldt, K. R., et al. 2005c, in *Protostars and Planets V*, Proceedings of the Conference held October 24-28, 2005, in Hilton Waikoloa Village, Hawai'i. LPI Contribution No. 1286, 8574
- Beichman, C. A., Tanner, A., Bryden, G., et al. 2006, *ApJ*, 639, 1166
- Beichman, C. A. & Velusamy, T. 1999, in *ASP Conf. Ser. 194: Working on the Fringe: Optical and IR Interferometry from Ground and Space*, 408
- Beichman, C. A., Woolf, N. J., & Lindensmith, C. A. 1999, *The Terrestrial Planet Finder (TPF) : a NASA Origins Program to Search for Habitable Planets (National Aeronautics and Space Administration : Jet Propulsion Laboratory publication ; 99-3)*
- Bernstein, R. A., Freedman, W. L., & Madore, B. F. 2002, *ApJ*, 571, 85
- Bowell, E. 1996, *VizieR Online Data Catalog*, 1, 2001
- Bracewell, R. N. 1978, *Nature*, 274, 780
- Brott, I. & Hauschildt, P. H. 2005, in *ESA SP-576: The Three-Dimensional Universe with Gaia*, ed. C. Turon, K. S. O’Flaherty, & M. A. C. Perryman, 565
- Brown, R. A. 2005, *ApJ*, 624, 1010

- Bryden, G., Beichman, C. A., Trilling, D. E., et al. 2006a, *ApJ*, 636, 1098
- Bryden, G., Tanner, A., Beichman, C. A., et al. 2006b, *ApJ*, in preparation
- Burns, J. A., Lamy, P. L., & Soter, S. 1979, *Icarus*, 40, 1
- Butler, R. P., Vogt, S. S., Marcy, G. W., et al. 2004, *ApJ*, 617, 580
- Carpenter et al., J. 2006, *ApJ*, in preparation
- Cayrel de Strobel, G., Soubiran, C., Friel, E. D., Ralite, N., & Francois, P. 1996, *VizieR Online Data Catalog*, 3200, 0
- Cayrel de Strobel, G., Soubiran, C., & Ralite, N. 2001, *VizieR Online Data Catalog*, 3221, 0
- Chen, Y. Q., Nissen, P. E., Benoni, T., & Zhao, G. 2001, *VizieR Online Data Catalog*, 337, 10943
- Decin, G., Dominik, C., Malfait, K., Mayor, M., & Waelkens, C. 2000, *A&A*, 357, 533
- Dermott, S. F. & Kehoe, T. J. J. 2004, in *ASP Conf. Ser. 324: Debris Disks and the Formation of Planets*, ed. L. Caroff, L. J. Moon, D. Backman, & E. Praton, 143
- Dominik, C. & Decin, G. 2003, *ApJ*, 598, 626
- Draine, B. T. & Lee, H. M. 1984, *ApJ*, 285, 89
- Eggen, O. J. 1998, *AJ*, 115, 2397
- Fajardo-Acosta, S. B., Beichman, C. A., & Cutri, R. M. 2000, *ApJ*, 538, L155
- Feltzing, S., Holmberg, J., & Hurley, J. R. 2001, *VizieR Online Data Catalog*, 337, 70911
- Fischer, D. A. & Valenti, J. 2005, *ApJ*, 622, 1102
- Giraud, P. and Lin, D. N. C. 2006, *ApJ*, submitted
- Gautier et al., T. N. 2006, *ApJ*, in preparation
- Giorgini, J. D. 2005, in <http://ssd.jpl.nasa.gov/ispy.html>
- Gonzalez, G. 1997, *MNRAS*, 285, 403
- Gordon, K. D., Rieke, G. H., Engelbracht, C. W., et al. 2005, *PASP*, 117, 503

- Gordon, K. D., Engelbracht, C. W., Muzerolle, J., et al. 2004, in *Microwave and Terahertz Photonics*. Edited by Stohr, Andreas; Jager, Dieter; Iezekiel, Stavros. Proceedings of the SPIE, Volume 5487,(2004)., ed. J. C. Mather, 177–185
- Habing, H. J., Bouchet, P., Dominik, C., et al. 1996, *A&A*, 315, L233
- Habing, H. J., Dominik, C., Jourdain de Muizon, M., et al. 2001, *A&A*, 365, 545
- Hauschildt, P. H., Allard, F., & Baron, E. 1999, *ApJ*, 512, 377
- Hayashi, C. 1981, *Progress of Theoretical Physics Supplement*, 70, 35
- Holmes, E. K., Dermott, S. F., & Gustafson, B. A. S. 2002, in *ESA SP-500: Asteroids, Comets, and Meteors: ACM 2002*, ed. B. Warmbein, 43–46
- Ibukiyama, A. & Arimoto, N. 2002, *VizieR Online Data Catalog*, 339, 40927
- Kalas, P., Graham, J. R., & Clampin, M. 2005, *Nature*, 435, 1067
- Kalas, P., Graham, J. R., Clampin, M. C., & Fitzgerald, M. P. 2006, *ApJ*, 637, L57
- Kasting, J. F., Whitmire, D. P., & Reynolds, R. T. 1993, *Icarus*, 101, 108
- Kelsall, T., Weiland, J. L., Franz, B. A., et al. 1998, *ApJ*, 508, 44
- Kim, J. S., Hines, D. C., Backman, D. E., et al. 2005, *ApJ*, 632, 659
- Kurucz, R. L. 2003, in *IAU Symposium*, 45
- Lachaume, R., Dominik, C., Lanz, T., & Habing, H. J. 1999, *A&A*, 348, 897
- Lambert, D. L. & Reddy, B. E. 2004, *VizieR Online Data Catalog*, 734, 90757
- Landgraf, M., Liou, J.-C., Zook, H. A., & Grün, E. 2002, *AJ*, 123, 2857
- Laughlin, G., Bodenheimer, P., & Adams, F. C. 2004, *ApJ*, 612, L73
- Laureijs, R. J., Jourdain de Muizon, M., Leech, K., et al. 2002, *A&A*, 387, 285
- Lawson, P., Unwin, S., & Beichman, C. A. 2004, in *JPL Technical Report, #04-014*, <http://planetquest.jpl.nasa.gov/documents/RdMp273.pdf>
- Lay, O. P. 2004, *Appl. Opt.*, 43, 6100

- Lay, O. P., Gunter, S. M., Hamlin, L. A., et al. 2005, in *Cryogenic Optical Systems and Instruments XI*. Edited by Heaney, James B.; Burriesci, Lawrence G. Proceedings of the SPIE, Volume 5905, 8–20
- Levison, H. F. & Morbidelli, A. 2003, *Nature*, 426, 419
- Mannings, V. & Barlow, M. J. 1998, *ApJ*, 497, 330
- Marcy, G. W., Butler, P. R., Frink, S., et al. 2002, in *Science with the Space Interferometry Mission*, 3
- Marcy, G. W., Butler, R. P., Fischer, D. A., & Vogt, S. S. 2004, in *ASP Conf. Ser. 321: Extrasolar Planets: Today and Tomorrow*, 3
- Marsakov, V. A. & Shevelev, Y. G. 1995, *VizieR Online Data Catalog*, 5089, 0
- Martin, S. R., Gappinger, R. O., Loya, F. M., et al. 2003, in *Techniques and Instrumentation for Detection of Exoplanets*. Edited by Coulter, Daniel R. Proceedings of the SPIE, Volume 5170, 144–154
- McKee, C. F. & Taylor, J. H. 2001, *S&T*, 101, 38
- Meyer, M. R., Hillenbrand, L. A., Backman, D. E., et al. 2004, *ApJS*, 154, 422
- Montes, D., López-Santiago, J., Gálvez, M. C., et al. 2001, *MNRAS*, 328, 45
- Moro-Martín, A. & Malhotra, R. 2005, *ApJ*, 633, 1150
- Nitschelm, C., Lecavelier des Etangs, A., Vidal-Madjar, A., et al. 2000, *A&AS*, 145, 275
- Nordstrom, B., Mayor, M., Andersen, J., et al. 2004, *VizieR Online Data Catalog*, 5117, 0
- Perrin, M.-N., de Strobel, G. C., Cayrel, R., & Hejlesen, P. M. 1977, *A&A*, 54, 779
- Plavchan, P., Jura, M., & Lipsky, S. J. 2005, *ApJ*, 631, 1161
- Randich, S., Gratton, R., Pallavicini, R., Pasquini, L., & Carretta, E. 1999, *A&A*, 348, 487
- Rieke, G. H., Su, K. Y. L., Stansberry, J. A., et al. 2005, *ApJ*, 620, 1010
- Rieke, G. H., Young, E. T., Engelbracht, C. W., et al. 2004, *ApJS*, 154, 25
- Rocha-Pinto, H. J. & Maciel, W. J. 1998, *A&A*, 339, 791
- Santos, N. C., Israelian, G., & Mayor, M. 2001, *A&A*, 373, 1019

- Sasselov, D. D. & Lecar, M. 2000, *ApJ*, 528, 995
- Shao, M., Baliunas, S., Boden, A., et al. 2002, in *Science with the Space Interferometry Mission*, 7
- Sheret, I., Dent, W. R. F., & Wyatt, M. C. 2004, *MNRAS*, 348, 1282
- Shevelev, Y. G. & Marsakov, V. A. 1988, *Bulletin d'Information du Centre de Donnees Stellaires*, 35, 131
- Spangler, C., Sargent, A. I., Silverstone, M. D., Becklin, E. E., & Zuckerman, B. 2001, *ApJ*, 555, 932
- Stapelfeldt, K. R., Holmes, E. K., Chen, C., et al. 2004, *ApJS*, 154, 458
- Stencel, R. E. & Backman, D. E. 1991, *ApJS*, 75, 905
- Stern, S. A. 1996, *A&A*, 310, 999
- Su, K. Y. L., Rieke, G. H., Misselt, K. A., et al. 2005, *ApJ*, 628, 487
- Su, K. Y. L., Rieke, G. H., et al. 2006, *ApJ*, submitted
- Taylor, B. J. 2002, *VizieR Online Data Catalog*, 339, 80731
- Traub, W. A., Kasting, J., Shao, M., Johnston, K. J., Beichman, C. A., 2006, in *IAU Colloquium #200*, Nice, France, in press.
- Valenti, J. A. & Fischer, D. A. 2005, *ApJS*, 159, 141
- Walker, H. J. & Wolstencroft, R. D. 1988, *PASP*, 100, 1509
- Werner, M. W., Roellig, T. L., Low, F. J., et al. 2004, *ApJS*, 154, 1
- Wright, J. T., Marcy, G. W., Butler, R. P., & Vogt, S. S. 2004, *ApJS*, 152, 261
- Wyatt, M. C., Greaves, J. S., Dent, W. R. F., & Coulson, I. M. 2005, *ApJ*, 620, 492

Table 1. Basic Data

Star	HIP	GJ	HR	other name	Spectral Type	V (mag)	K (mag)	Mo/W/Average ^a	Age (Gyr)		# est.	References	Average	[Fe/H]	References
									Min	Max				σ	
GL 436 ^b	57087	436			M2.5	10.67	6.07	—	—	—	0	—	—	—	—
GL 908	117473	908		BR Psc	M1	8.98	5.04	—	—	—	0	—	—	—	—
HD 739	950	3013	35	θ Scl	F4V	5.24	4.13 ^d	2.80	2.40	3.19	2	I,N	-0.13	0.07	CS,E,I,M,N
HD 4391	3583	1021	209		G5IV	5.80	4.30 ^d	12.30	—	—	1	N	-0.17	0.07	E,N,RP
HD 4813	3909	37	235	19 Cet	F7IV-V	5.17	4.02 ^d	5.04	2.35	9.63	7	C,I,L,La,N,P	-0.16	0.09	CS,C,E,I,L,La
HD 10360 ^c		66B	486		K2V	5.76	3.56 ^d	0.15	—	—	1	Mo	-0.23	0.03	E,N,RP
HD 16895	12777	107A	799	θ Per	F7V	4.10	2.98 ^e	5.01	2.50	7.94	5	W,C,L,N,P	-0.08	0.09	CS,C,E,L,M,N
HD 20794	15510	139	1008	e Eri	G8V	4.26	2.52 ^e	—	—	—	0	—	-0.32	0.09	CS,E,I,N,P
HD 22001		143.2A	1083	κ Ret	F5IV-V	4.71	3.94 ^d	0.60	0.60	9.38	5	Mo,La,N	-0.13	0.07	CS,La,M,N
HD 23249	17378	150	1136	δ Eri	K0IV	3.52	1.45 ^e	12.59	—	—	1	P	0.02	0.11	CS,P,RP
HD 23754	17651	155	1173	27 Eri	F3/F5V	4.22	3.35 ^d	2.01	1.40	3.02	4	F,I,M,N	0.05	0.08	CS,F,I,M,N
HD 25998	19335	161	1278	50 Per	F7V	5.52	4.28 ^d	0.60	0.60	5.14	4	Mo,C,L,N	-0.01	0.10	CS,C,L,M,N
HD 28343	20917	169			K7V	8.30	4.88	—	—	—	0	—	—	—	—
HD 32147	23311	183	1614		K3V	6.22	3.71 ^d	—	—	—	0	—	0.16	0.14	CS,E,I,P
HD 36395	25878	205			M1.5V	7.97	3.86 ^e	—	—	—	0	—	0.60	—	CS
HD 38392 ^c		216B	1982	γ Lep B	K2V	6.15	4.13 ^d	8.94	8.75	9.14	3	La	-0.05	0.09	CS,E,La,M,N
HD 38858	27435	1085	2007		G4V	5.97	4.41 ^d	4.57	3.19	12.20	3	W,I,N	-0.25	0.01	I,N,T
HD 39587	27913	222	2047	54 Ori	G0V	4.39	2.97 ^e	6.60	0.10	10.70	5	B,C,L,N,P	-0.07	0.07	CS,C,E,L,M,N
HD 40136	28103	225	2085	η Lep	F1V	3.71	2.90 ^e	1.31	1.22	1.41	3	I,N,P	-0.16	0.06	CS,I,M,N
HD 46588	32439	240	2401		F8V	5.44	4.14 ^d	5.13	4.27	6.20	4	B,F,I,N	-0.22	0.07	F,I,M,N
HD 48682	32480	245	2483	56 Aur	G0V	5.24	4.13 ^d	3.31	3.31	8.91	5	W,B,M,N,P	0.07	0.08	CS,E,M,N
HD 50281 ^c	32984	250A			K3V	6.58	4.11 ^d	9.42	9.02	9.82	3	La	0.06	0.07	CS,La,M,N
HD 53706 ^c	34069	264.1B	2668		K0V	6.83	4.94	—	—	—	0	—	-0.24	0.05	CS,E,N,RP
HD 55892	34834	268	2740	QW Pup	F0IV	4.49	3.71 ^{d,e}	1.78	1.40	2.16	2	L,N	-0.30	0.10	CS,L,M,N
HD 62644	37606		2998	GJ 284	G6IV	5.04	3.12 ^d	7.17	3.41	14.13	3	I,P,R	-0.09	0.21	CS,I,P,R
HD 63077	37853	288A	3018	171 Pup	G0V	5.36	3.75 ^d	5.01	5.01	14.50	4	W,C,I,N	-0.79	0.11	CS,C,E,I,M,N
HD 67228	39780		3176	μ Cnc	G2IV	5.30	3.83 ^e	8.32	5.50	8.32	4	W,F,I,N	0.11	0.06	CS,F,I,N
HD 68146	40035	297.2A	3202	18 Pup	F7V	5.53	4.35 ^d	4.18	2.92	5.19	4	C,L,M,N	-0.13	0.10	CS,C,E,L,M,N
HD 71243	40702	305	3318	α Cha	F5V	4.05	3.15 ^d	1.47	1.40	1.53	2	F,N	0.07	0.02	F,M,N
HD 72673	41926	309	3384		K0V	6.38	4.44 ^d	4.57	—	—	1	W	-0.36	0.06	CS,E,I,N,RP
HD 76653	43797	3519	3570		F6V	5.70	4.56 ^d	2.31	2.10	2.52	2	I,N	-0.04	0.07	I,M,N
HD 76932	44075	3523	3578		F7/F8IV/V	5.80	4.36 ^d	11.00	9.29	12.50	4	C,F,I,N	-0.84	0.12	CS,C,E,F,I,L
HD 78366	44897	334	3625		F9V	5.95	4.55	5.17	3.84	6.50	2	I,N	0.02	0.09	E,I,M,N
HD 79211 ^c	120005	338B			K2	7.70	4.14 ^e	—	—	—	0	—	—	—	—

Table 1—Continued

Star	HIP	GJ	HR	other name	Spectral Type	V (mag)	K (mag)	Mo/W/Average ^a			Age (Gyr)			References	Average	[Fe/H]		Reference
								Mo	W	Average ^a	Min	Max	# est.			Average	σ	
HD 81937	46733	3559	3757	h UMa	F0IV	3.65	2.82 ^{d,e}	0.90	—	—	1	N	0.06	—	N			
HD 81997	46509	348A	3759	31 Hya	F6V	4.59	3.56 ^d	6.38	1.94	9.43	5	La,M,N	0.00	0.01	E,La,M,N			
HD 85512	48331			GJ 370	K5V	7.67	4.72	0.30	—	—	1	Mo	—	—	—			
HD 89449	50564	388	4054	40 Leo	F6IV	4.78	3.65 ^{d,e}	2.31	1.64	3.40	4	F,I,M,N	0.02	0.08	CS,F,I,M,N			
HD 90089	51502	392	4084		F2V	5.25	4.27 ^d	1.78	1.50	2.06	2	I,N	-0.28	0.10	I,M,N,T			
HD 90589	50954	391	4102	I Car	F2IV	3.99	3.12 ^e	1.73	0.40	3.33	3	I,M,N	0.01	0.14	I,M,N			
HD 91324	51523	397	4134		F6V	4.89	3.58 ^d	5.39	4.28	7.94	4	L,M,N,P	-0.54	0.35	CS,L,M,N			
HD 100623	56452	432A	4458		K0V	5.96	4.02 ^d	3.72	3.72	10.08	4	W,La	-0.38	0.10	E,La,M,N,RP			
HD 102365	57443	442A	4523		G5V	4.89	3.31 ^e	8.95	6.12	10.08	4	I,La	-0.36	0.14	CS,E,I,La,N,P			
HD 103095	57939	451A	4550	CF UMa	G8V	6.42	4.37 ^e	3.24	3.24	5.40	2	W,B	-1.35	0.02	CS,E,N,P,T			
HD 105211	59072	455	4616	η Cru	F2V	4.14	3.20 ^d	2.53	1.30	3.99	3	F,I,N	-0.37	0.18	I,M,N			
HD 105452	59199	455	4623	α Crv	F0IV/V	4.02	3.17 ^e	2.82	—	—	1	P	-0.43	0.26	CS,N,P			
HD 109085	61174	471	4775	η Crv	F2V	4.30	3.54 ^e	1.27	0.95	1.56	3	I,M,N	-0.05	0.04	I,M,N			
HD 129502	71957	9491	5487	μ Vir	F2V	3.87	2.90 ^e	1.29	0.71	1.71	4	F,I,M,N	0.03	0.09	F,I,M,N			
HD 131977 ^c	73184	570A	5568		K4V	5.72	3.15 ^e	—	—	—	0	—	0.07	0.07	CS,P,RP,T			
HD 132254	73100	3880	5581		F7V	5.63	4.41	3.35	2.16	3.96	6	C,F,I,L,M,N	0.01	0.05	CS,C,F,L,M,N			
HD 136352 S	75181	582	5699		G2V	5.65	4.16 ^d	11.71	7.52	15.90	2	I,N	-0.36	0.08	CS,E,I,N,P,R			
HD 139664	76829	594	5825	g Lup	F5IV-V	4.64	3.80 ^d	0.15	0.15	9.30	6	Mo,I,La,N	-0.15	0.09	I,La,M,N			
HD 142267	77801	3924	5911	39 Ser	G0V	6.07	4.53 ^d	3.24	3.24	13.50	3	W,N,P	-0.34	0.14	CS,E,M,N,P			
HD 147513 ^b	80337	620.1A	6094		G5V	5.37	3.93 ^e	0.30	0.30	8.50	2	Mo,N	0.02	0.11	CS,M,N,RP			
HD 151288	82003	638			K7V	8.10	4.71	—	—	—	0	—	—	—	—			
HD 154363	83591	653			K5V	7.70	4.73	—	—	—	0	—	—	—	—			
HD 156026	84478	664		36 Oph C	K5V	6.33	3.47 ^d	8.80	8.64	8.96	3	La	-0.16	0.07	CS,La,P			
HD 157881	85295	673			K7V	7.54	4.14 ^e	9.34	—	—	1	La	0.00	0.35	CS,I			
HD 158633	85235	675	6518		K0V	6.44	4.52 ^d	4.27	—	—	1	W	-0.43	0.08	E,I,M,N			
HD 160032	86486	686	6569	λ Ara	F3IV	4.76	3.83 ^d	2.44	1.85	3.30	4	F,I,M,N	-0.29	0.06	CS,F,I,M,N			
HD 164259	88175	699	6710	ζ Ser	F3V	4.62	3.64 ^d	1.78	1.34	2.06	5	F,I,L,M,N	-0.11	0.06	CS,F,I,L,M			
HD 165499	89042	705	6761	<i>i</i> Pav	G1V	5.47	4.13 ^d	6.27	2.65	10.80	4	I,L,M,N	-0.14	0.07	CS,E,I,L,M,I			
HD 172051	91438	722	6998		G5V	5.85	4.23 ^d	3.89	1.54	3.89	2	W,I	-0.28	0.03	E,I,N,RP			
HD 177565	93858	744	7232		G8V	6.15	4.54 ^d	8.04	5.01	13.20	3	I,N,R	0.05	0.02	CS,E,I,N,R,R			
HD 180617	94761	752A			M2.5	9.12	4.67 ^e	—	—	—	0	—	—	—	—			
HD 182488	95319	758	7368		G8V	6.37	4.49 ^d	4.47	4.47	10.52	2	W,I	0.11	0.08	E,I,M,N,RP			
HD 185395	96441	765A	7469	θ Cyg	F4V	4.49	3.54 ^d	6.53	1.50	9.24	5	La,N,P	-0.04	0.08	CS,La,M,N,P			
HD 187691	97675	768.1A	7560	<i>o</i> Aql	F8V	5.12	3.90 ^d	6.61	3.70	9.00	6	W,B,C,L,M,N	0.09	0.04	CS,C,L,M,N			

Lambert & Reddy (2004); (La) Lachaume et al. (1999); (M) Shevelev & Marsakov (1988); Marsakov & Shevelev (1995); (Mo) Montes et al. (2001); (N) Nordstrom et al. (2004); (P) L. (1977); (R) Randich et al. (1999); (RP) Rocha-Pinto & Maciel (1998); (T) Taylor (2002); (W) Wright et al. (2004); (V) Valenti & Fischer (2005)

Table 2. Measured and predicted flux densities at 24 and 70 μm (in mJy)

Star	24 μm				70 μm					
	$F_{\nu, MIPS}$	$F_{\nu, *}$	$F_{\nu, MIPS}/F_{\nu, *}$	χ_{24}^a	$F_{\nu, MIPS}$	$F_{\nu, *}$	$F_{\nu, MIPS}/F_{\nu, *}$	S/N	χ_{70}^b	L_{dust}/L_*^c
GL 436	38.7	31.3	1.24	6.0	4.0 \pm 2.2	3.5	1.1	1.9	0.2	$< 5.4 \times 10^{-5}$
GL 908	96.3	99.2	0.97	-0.7	12.0 \pm 3.3	10.9	1.1	4.3	0.3	$< 2.2 \times 10^{-5}$
HD 739	159.1	142.5	1.12	1.4	16.2 \pm 3.8	16.2	1.0	5.6	0.0	$< 3.3 \times 10^{-6}$
HD 4391	141.3	150.7	0.94	-1.6	19.5 \pm 3.5	17.2	1.1	8.4	0.7	$< 3.9 \times 10^{-6}$
HD 4813	191.8	207.3	0.93	-0.9	21.2 \pm 4.6	23.5	0.9	7.2	-0.5	$< 2.7 \times 10^{-6}$
HD 10360	247.7	283.6	0.87	-1.6	23.1 \pm 6.1	32.4	0.7	6.3	-1.5	$< 4.6 \times 10^{-6}$
HD 16895	492.7	458.7	1.07	1.9	51.2 \pm 9.7	51.9	1.0	8.8	-0.1	$< 2.4 \times 10^{-6}$
HD 20794	737.2	770.8	0.96	-1.1	94.3 \pm 13.6	87.9	1.1	28.7	0.5	$< 1.2 \times 10^{-6}$
HD 22001	233.7	205.8	1.14	1.7	25.2 \pm 4.8	23.3	1.1	7.8	0.4	$< 2.7 \times 10^{-6}$
HD 23249	2039.1	1825.2	1.12	2.9	207.0 \pm 32.1	206.5	1.0	24.5	0.0	$< 1.5 \times 10^{-6}$
HD 23754	383.3	368.0	1.04	0.5	46.6 \pm 7.1	41.8	1.1	13.8	0.7	$< 1.5 \times 10^{-6}$
HD 25998 ^{d,e}	147.1	128.5	1.14	3.6	61.9 \pm 5.7	14.5	4.3	11.7	8.3	2.7×10^{-5}
HD 28343	85.4	98.4	0.87	-3.3	-9.5 \pm 14.8	11.4	-0.8	-0.6	-1.4	$< 8.8 \times 10^{-5}$
HD 32147	224.3	240.6	0.93	-0.8	23.1 \pm 6.3	27.5	0.8	4.9	-0.7	$< 7.6 \times 10^{-6}$
HD 36395	250.7	288.9	0.87	-3.3	26.7 \pm 17.6	30.2	0.9	1.6	-0.2	$< 4.9 \times 10^{-5}$
HD 38392	203.7	156.9	1.30	3.7	18.8 \pm 8.2	17.7	1.1	2.4	0.1	$< 1.8 \times 10^{-5}$
HD 38858 ^{e,f}	131.3	131.3	1.00	0.0	153.7 \pm 9.8	15.0	10.3	16.0	14.1	1.0×10^{-4}
HD 39587	483.6	488.5	0.99	-0.3	35.3 \pm 12.1	55.4	0.6	4.0	-1.7	$< 4.0 \times 10^{-6}$
HD 40136 ^{d,e}	553.3	490.5	1.13	3.2	90.7 \pm 9.4	55.6	1.6	21.3	3.7	4.0×10^{-6}
HD 46588	150.8	161.8	0.93	-1.7	14.6 \pm 3.7	18.3	0.8	6.1	-1.0	$< 3.0 \times 10^{-6}$
HD 48682 ^{e,f}	188.4	188.8	1.00	0.0	256.9 \pm 6.8	21.3	12.1	46.3	36.8	1.1×10^{-4}
HD 50281	175.8	174.5	1.01	0.2	17.1 \pm 5.4	19.9	0.9	3.8	-0.5	$< 10.0 \times 10^{-6}$
HD 53706	72.5	73.4	0.99	-0.3	7.0 \pm 2.7	8.3	0.8	3.0	-0.5	$< 1.0 \times 10^{-5}$
HD 55892	263.8	243.0	1.09	2.1	25.5 \pm 5.7	27.6	0.9	6.6	-0.4	$< 2.2 \times 10^{-6}$
HD 62644	370.6	369.0	1.00	0.1	46.2 \pm 8.5	41.9	1.1	8.2	0.5	$< 4.0 \times 10^{-6}$
HD 63077	226.4	240.9	0.94	-1.5	15.6 \pm 8.0	27.6	0.6	2.3	-1.5	$< 6.2 \times 10^{-6}$
HD 67228	215.6	208.3	1.04	0.9	14.4 \pm 5.0	23.5	0.6	4.0	-1.8	$< 4.1 \times 10^{-6}$
HD 68146	132.6	132.5	1.00	0.0	18.3 \pm 3.6	15.1	1.2	6.6	0.9	$< 4.0 \times 10^{-6}$
HD 71243	451.1	434.5	1.04	0.5	52.9 \pm 8.2	49.3	1.1	14.5	0.4	$< 1.5 \times 10^{-6}$
HD 72673	119.2	132.8	0.90	-2.6	9.2 \pm 3.0	15.2	0.6	4.6	-2.0	$< 4.8 \times 10^{-6}$
HD 76653	112.3	109.1	1.03	0.7	33.9 \pm 10.5	12.4	2.7	3.3	2.1	$< 1.7 \times 10^{-5}$
HD 76932	130.2	140.7	0.93	-1.9	15.2 \pm 3.8	16.1	0.9	5.3	-0.2	$< 3.9 \times 10^{-6}$
HD 78366	108.3	115.3	0.94	-1.5	16.8 \pm 4.2	13.1	1.3	4.6	0.9	$< 6.8 \times 10^{-6}$
HD 79211	195.4	187.1	1.04	1.1	18.0 \pm 4.0	21.4	0.8	7.4	-0.8	$< 4.7 \times 10^{-6}$

Table 2—Continued

Star	24 μm				70 μm					
	$F_{\nu, MIPS}$	$F_{\nu, *}$	$F_{\nu, MIPS}/F_{\nu, *}$	χ_{24}^a	$F_{\nu, MIPS}$	$F_{\nu, *}$	$F_{\nu, MIPS}/F_{\nu, *}$	S/N	χ_{70}^b	L_{dust}/L_{\star}^c
HD 81937	563.9	558.4	1.01	0.2	70.0 ± 10.4	63.3	1.1	16.6	0.6	$< 1.0 \times 10^{-6}$
HD 81997	287.8	264.4	1.09	1.1	28.2 ± 5.7	30.0	0.9	8.0	-0.3	$< 2.4 \times 10^{-6}$
HD 85512	95.9	110.9	0.86	-3.4	11.0 ± 3.0	12.8	0.9	4.7	-0.6	$< 1.0 \times 10^{-5}$
HD 89449	240.8	255.1	0.94	-1.4	24.6 ± 5.3	28.9	0.8	8.2	-0.8	$< 2.1 \times 10^{-6}$
HD 90089 ^e	147.0	146.7	1.00	0.0	38.2 ± 3.6	16.7	2.3	14.9	6.0	8.5×10^{-6}
HD 90589	422.9	409.8	1.03	0.8	53.7 ± 8.5	46.4	1.2	11.0	0.9	$< 1.8 \times 10^{-6}$
HD 91324	263.2	273.9	0.96	-0.5	50.5 ± 9.2	31.2	1.6	6.4	2.1	$< 5.3 \times 10^{-6}$
HD 100623	183.8	193.4	0.95	-1.2	21.8 ± 4.1	22.1	1.0	9.0	-0.1	$< 4.0 \times 10^{-6}$
HD 102365	353.9	353.4	1.00	0.0	34.0 ± 8.5	40.2	0.8	5.7	-0.7	$< 4.1 \times 10^{-6}$
HD 103095	128.5	133.8	0.96	-1.0	9.3 ± 3.1	15.4	0.6	4.4	-1.9	$< 4.4 \times 10^{-6}$
HD 105211 ^{e, f}	367.9	363.4	1.01	0.2	473.7 ± 19.8	41.4	11.4	25.2	21.8	6.9×10^{-5}
HD 105452	396.9	409.1	0.97	-0.7	43.3 ± 8.4	46.6	0.9	9.3	-0.4	$< 1.6 \times 10^{-6}$
HD 109085 ^{d, e, f}	589.2	296.8	1.99	24.6	198.2 ± 6.8	33.5	5.9	42.7	24.0	3.3×10^{-5}
HD 129502	536.0	521.1	1.03	0.7	51.8 ± 9.7	59.1	0.9	13.1	-0.8	$< 1.2 \times 10^{-6}$
HD 131977	427.8	397.4	1.08	1.9	37.6 ± 7.4	45.3	0.8	12.6	-1.0	$< 3.2 \times 10^{-6}$
HD 132254	127.5	131.5	0.97	-0.8	23.6 ± 3.4	14.9	1.6	9.1	2.5	$< 3.8 \times 10^{-6}$
HD 136352	169.8	175.1	0.97	-0.8	17.5 ± 5.1	19.9	0.9	4.2	-0.5	$< 5.5 \times 10^{-6}$
HD 139664 ^{e, f}	275.9	251.9	1.10	1.2	503.7 ± 9.2	28.6	17.6	62.2	51.9	1.3×10^{-4}
HD 142267	111.4	107.5	1.04	0.9	9.5 ± 2.7	12.2	0.8	4.7	-1.0	$< 4.2 \times 10^{-6}$
HD 147513	201.1	195.4	1.03	0.7	17.3 ± 12.1	22.1	0.8	1.5	-0.4	$< 1.4 \times 10^{-5}$
HD 151288	102.7	115.9	0.89	-2.8	13.1 ± 2.7	13.4	1.0	7.4	-0.1	$< 9.0 \times 10^{-6}$
HD 154363	95.3	110.5	0.86	-3.4	9.7 ± 4.2	12.7	0.8	2.6	-0.7	$< 1.6 \times 10^{-5}$
HD 156026	304.2	306.9	0.99	-0.1	30.6 ± 10.9	35.2	0.9	3.2	-0.4	$< 1.5 \times 10^{-5}$
HD 157881	171.3	192.8	0.89	-2.8	13.1 ± 5.5	22.2	0.6	3.0	-1.7	$< 1.3 \times 10^{-5}$
HD 158633 ^e	112.3	125.1	0.90	-2.6	56.7 ± 3.6	14.4	3.9	19.9	11.8	4.1×10^{-5}
HD 160032	243.8	229.4	1.06	0.8	44.3 ± 6.1	26.1	1.7	9.4	3.0	$< 3.3 \times 10^{-6}$
HD 164259	246.4	226.0	1.09	1.1	8.3 ± 7.0	25.6	0.3	1.4	-2.5	$< 4.1 \times 10^{-6}$
HD 165499	174.4	182.1	0.96	-0.5	15.9 ± 4.5	20.6	0.8	4.9	-1.1	$< 4.1 \times 10^{-6}$
HD 172051	150.2	147.4	1.02	0.5	25.5 ± 11.5	16.7	1.5	2.3	0.8	$< 1.9 \times 10^{-5}$
HD 177565	110.9	109.8	1.01	0.2	16.4 ± 4.9	12.4	1.3	3.6	0.8	$< 1.2 \times 10^{-5}$
HD 180617	138.4	111.6	1.24	6.0	5.9 ± 13.4	12.7	0.5	0.4	-0.5	$< 9.6 \times 10^{-5}$
HD 182488	109.4	108.7	1.01	0.2	2.2 ± 10.7	12.3	0.2	0.2	-0.9	$< 2.7 \times 10^{-5}$
HD 185395	284.9	254.5	1.12	1.5	34.0 ± 5.3	28.8	1.2	11.1	1.0	$< 2.0 \times 10^{-6}$
HD 187691	212.0	211.5	1.00	0.0	21.0 ± 6.8	23.9	0.9	3.6	-0.4	$< 5.6 \times 10^{-6}$

Table 2—Continued

Star	24 μm				70 μm				L_{dust}/L_{\star}^c	
	$F_{\nu, MIPS}$	$F_{\nu, \star}$	$F_{\nu, MIPS}/F_{\nu, \star}$	χ_{24}^a	$F_{\nu, MIPS}$	$F_{\nu, \star}$	$F_{\nu, MIPS}/F_{\nu, \star}$	S/N		χ_{70}^b
HD 189245	120.8	116.5	1.04	0.9	6.6 ± 3.9	13.3	0.5	1.9	-1.7	$< 5.6 \times 10^{-6}$
HD 190406	126.6	133.0	0.95	-1.2	22.6 ± 5.1	15.1	1.5	5.0	1.5	$< 7.9 \times 10^{-6}$
HD 191849	179.0	192.8	0.93	-1.8	26.9 ± 4.1	21.2	1.3	10.3	1.4	$< 9.8 \times 10^{-6}$
HD 192310	250.4	236.4	1.06	0.7	19.1 ± 5.6	26.8	0.7	5.0	-1.4	$< 6.3 \times 10^{-6}$
HD 196877	54.1	59.4	0.91	-2.2	2.2 ± 2.2	6.8	0.3	1.1	-2.1	$< 2.0 \times 10^{-5}$
HD 198149	2444.6	2418.4	1.01	0.3	254.6 ± 42.0	276.7	0.9	38.5	-0.5	$< 8.6 \times 10^{-7}$
HD 199260 ^{d,e}	120.1	108.5	1.11	2.7	42.8 ± 4.1	12.3	3.5	11.7	7.4	2.1×10^{-5}
HD 213845	158.7	144.7	1.10	1.2	23.9 ± 4.0	16.4	1.5	7.5	1.9	$< 4.3 \times 10^{-6}$
HD 215648	505.7	516.7	0.98	-0.3	47.4 ± 9.6	58.8	0.8	12.7	-1.2	$< 1.4 \times 10^{-6}$
HD 217357	133.4	139.3	0.96	-1.1	18.6 ± 3.5	16.1	1.2	7.5	0.7	$< 8.6 \times 10^{-6}$
HD 219482 ^{d,e}	140.9	131.0	1.08	1.9	65.4 ± 3.7	14.9	4.4	22.5	13.8	2.8×10^{-5}
HD 219623 ^e	144.6	139.7	1.04	0.9	48.0 ± 3.8	15.8	3.0	15.9	8.4	1.7×10^{-5}
HD 222237	108.4	112.0	0.97	-0.8	20.5 ± 2.8	12.8	1.6	9.9	2.7	$< 7.1 \times 10^{-6}$
HD 265866	84.8	95.2	0.89	-2.7	—	9.9	—	—	—	—
Companions										
HD 10360J	241.0	337.7	0.71	-3.6	23.8 ± 6.8	38.2	0.6	6.5	-2.1	$< 3.5 \times 10^{-6}$
HD 38393	765.4	761.6	1.00	0.1	57.3 ± 15.1	86.4	0.7	7.3	-1.9	$< 2.0 \times 10^{-6}$
HD 50281B	55.3	43.7	1.26	6.6	10.1 ± 4.6	5.0	2.0	2.2	1.1	$< 8.3 \times 10^{-5}$
HD 53705	166.4	192.1	0.87	-3.3	17.3 ± 4.0	21.9	0.8	7.3	-1.1	$< 3.0 \times 10^{-6}$
HD 79210	191.4	260.3	0.74	-6.6	21.4 ± 5.1	29.8	0.7	8.8	-1.6	$< 5.6 \times 10^{-6}$
HD 131976	274.4	246.8	1.11	2.8	15.6 ± 5.2	28.2	0.6	5.2	-2.4	$< 9.2 \times 10^{-6}$

^aSignificance of 24 μm excess (eq. [1])

^bSignificance of 70 μm excess (eq. [2])

^cMinimum L_{dust}/L_{\star} from 70 μm emission (eq. [3])

^dStar with excess 24 μm emission

^eStar with excess 70 μm emission

^fStar with resolved 70 μm emission

Table 3. IRAC Observations of M Stars^a

Star	Spectral Type	$F_\nu(3.55 \mu\text{m})$ (Jy)	$F_\nu(4.49 \mu\text{m})$ (Jy)	$F_\nu(5.73 \mu\text{m})$ (Jy)	$F_\nu(7.87 \mu\text{m})$ (Jy)
GL908	M1	3.29	2.22	1.43	0.82
HD 36395	M1.5V	7.64	5.62	3.74	2.22
HD 191849	K7/M0	6.46	4.12	2.70	1.58
HD 265866	M3.5	2.75	1.83	1.22	0.70

^aFlux density uncertainties are dominated by calibration uncertainties, typically 5% for the IRAC bands.

Table 4. Dust Emission at 24 and 70 μm (in mJy)

Star	$F_\nu(24)_{dust}$	$F_\nu(70)_{dust}^a$	T_{dust}^b	L_{dust}/L_\star^c
HD 25998	18.6 ± 5.9	51.1 ± 9.6	96 ± 5	4.5×10^{-5}
HD 38858 ^d	$< 15 (3\sigma)$	193 ± 25	< 70	12×10^{-5}
HD 40136	63 ± 22	37.9 ± 11	165_{-20}^{+35}	1.9×10^{-5}
HD 48682 ^d	$< 22 (3\sigma)$	290 ± 38	< 68	1.1×10^{-4}
HD 90089	$< 18 (3\sigma)$	23.2 ± 5.0	< 120	0.8×10^{-5}
HD 105211 ^d	$< 45 (3\sigma)$	521 ± 73	< 70	7.3×10^{-5}
HD 109085 ^d	292 ± 24	212 ± 28	150 ± 10	15×10^{-5}
HD 139664 ^d	$< 75 (3\sigma)$	523 ± 77	< 78	12×10^{-5}
HD 158633	$< 13 (3\sigma)$	45.8 ± 7.8	< 90	3.5×10^{-5}
HD 199260	11.6 ± 5.6	32.9 ± 6.4	94 ± 5	3.3×10^{-5}
HD 219482	9.8 ± 5.6	54.5 ± 9.0	81 ± 3	3.6×10^{-5}
HD 219623	$< 17 (3\sigma)$	34.8 ± 6.5	< 104	1.6×10^{-5}

^aDust fluxes at 70 μm have been color corrected by 8%.

^bBlackbody temperature based on either the 24 to 70 μm flux density ratio or the 70 μm flux density plus a 3σ upper limit at 24 μm .

^cIf only 70 μm data are available, L_{dust}/L_\star is from Eqn 3. If 24 μm and 70 μm data are available, L_{dust}/L_\star obtained from Eqn 4.

^dFor the resolved sources, the emission is fit with an extended Gaussian profile, resulting in measured dust fluxes $\sim 10\%$ higher than from the standard aperture photometry.

Table 5. Parameters for TPF S/N Calculations

Parameter	TPF-C	TPF-I
Wavelength	0.55 μm	12 μm
Telescope	3.5x8m	Four, 3m on 75 m baseline
Beam Half Width	39x17 mas	500 mas
Beam Area, Ω_{tel}	5×10^{-14}	1.8×10^{-11}
Local Zodiacal Emission (I_{LZ})	0.1 MJy sr $^{-1}$	12 MJy sr $^{-1}$
Zodiacal Flux Density ($I_{LZ}\Omega_{tel}$)	5 nJy	220 μJy
Stellar Magnitude ^a	V=4.5 mag (60 Jy)	[12]=3.0 mag (1.7 Jy)
Stellar Rejection	10^{-10}	10^{-5}
Stellar Leakage Signal	6 nJy	17 μJy
Planet Brightness	6 nJy	0.3 μJy

^afor a Solar twin at 10 pc.

Table 6. Predicted Dust Emission at 10 μm

Star	F_ν (mJy)	Exo-Zodi ^a (Solar System = 1)
HD 25998	0.041	1.7
HD 40136	5.1	42
HD 109085	23	325
HD 199260	0.024	1.1
HD 219482	0.004	0.2

^a L_{dust}/L_\star at 10 μm in units of 10^{-7} , corresponding roughly to that of the Solar System (Backman & Paresce 1993). See eq. [2] of Beichman et al. (2006).

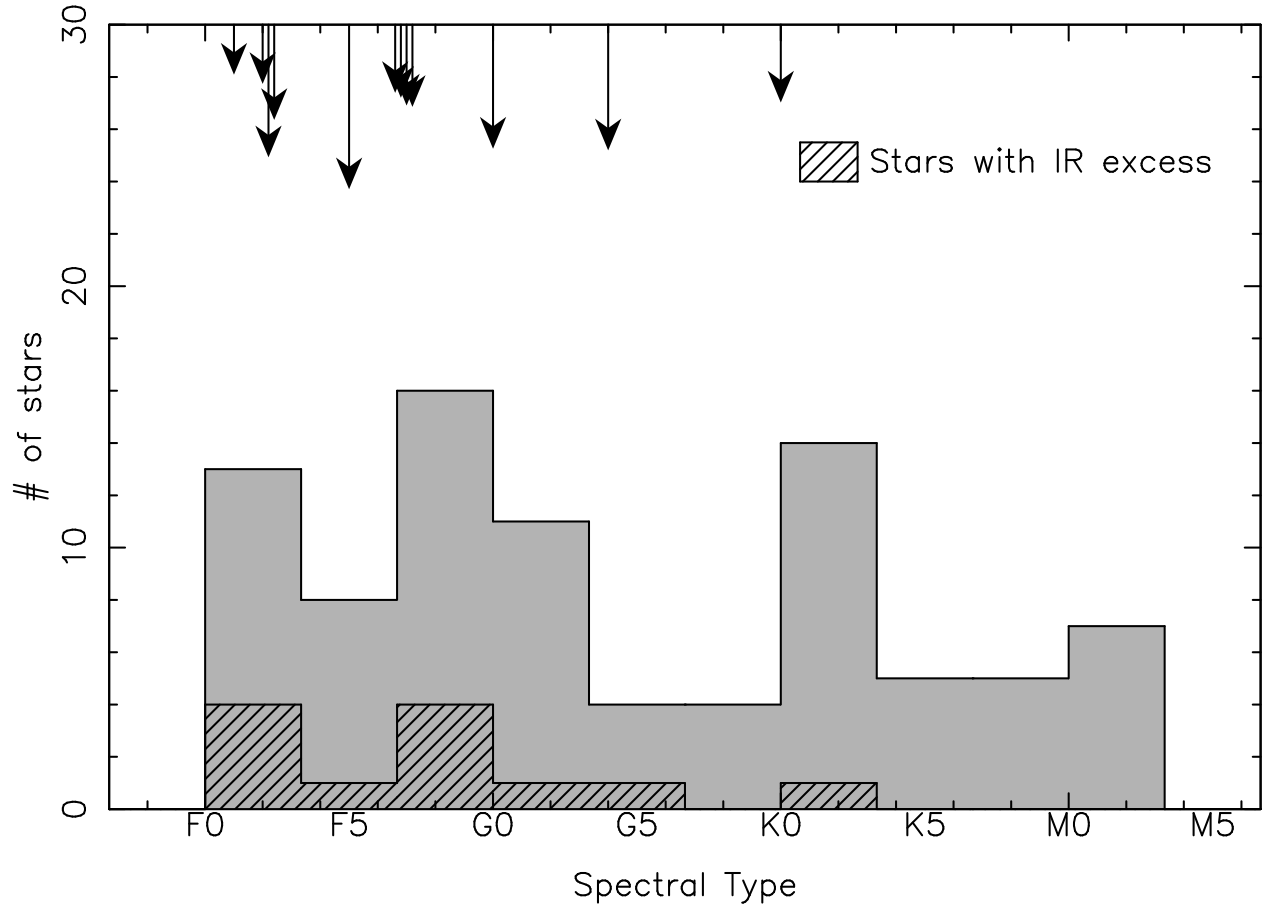


Fig. 1.— Spectral type distribution for stars in this SIM/TPF sample. The spectral types of stars found to have $70 \mu\text{m}$ excess are highlighted within the histogram (slant-hash) and are individually flagged with arrows at the top of the plot. The length of each arrow is an indicator of the strength of $70 \mu\text{m}$ excess relative to the stellar photosphere. We find that $70 \mu\text{m}$ excess is more readily detected around early type stars.

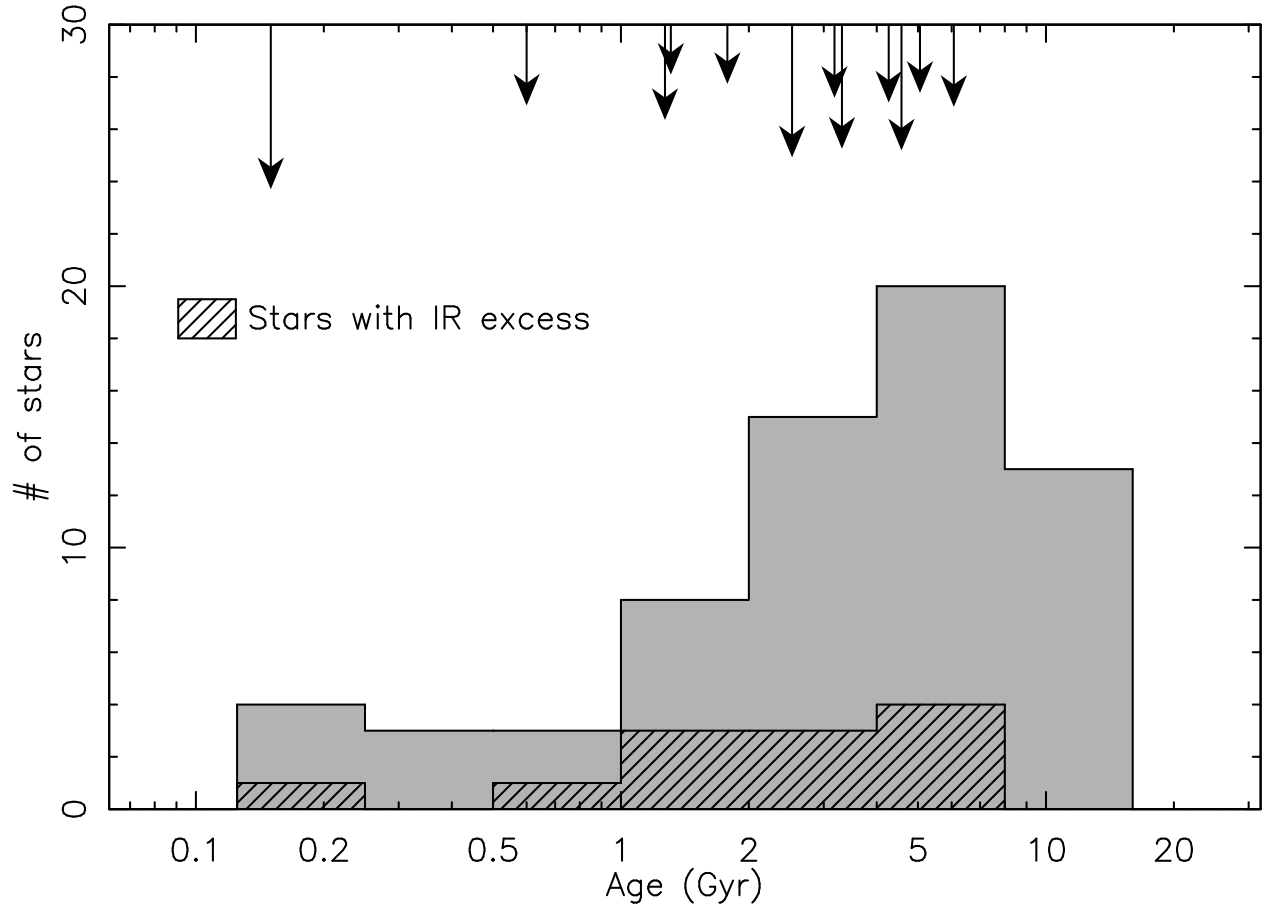


Fig. 2.— Age distribution for stars in this SIM/TPF sample. The ages of stars with $70\ \mu\text{m}$ excess are highlighted within the histogram (slant-hash) and are individually flagged with arrows at the top of the plot. The length of each arrow is an indicator of the strength of $70\ \mu\text{m}$ excess. There is a weak correlation between the detection of IR excess and the stellar age, with no stars older than 7 Gyr having excess emission.

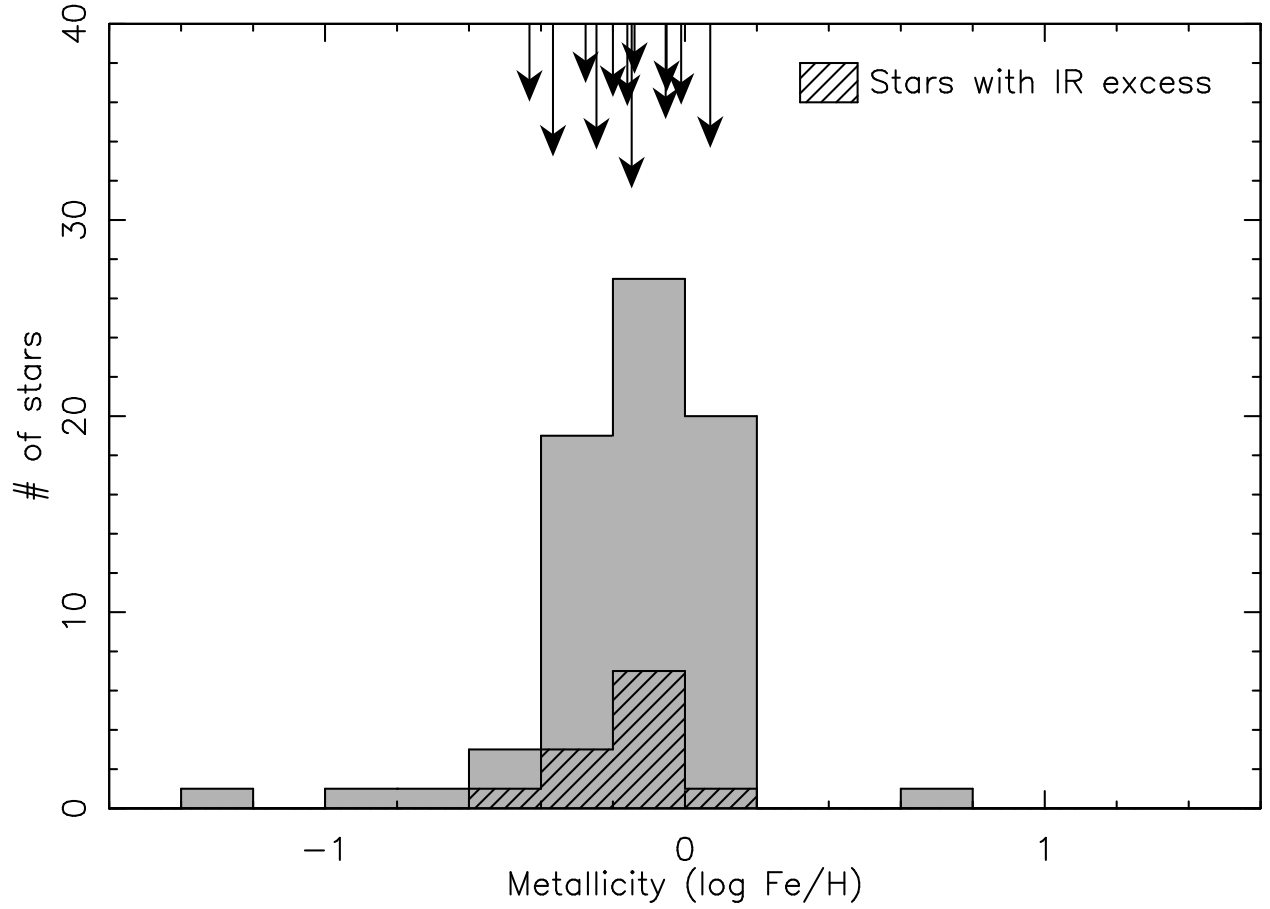


Fig. 3.— Metallicity distribution for stars in this SIM/TPF sample. The ages of stars with $70\ \mu\text{m}$ excess are highlighted within the histogram (slant-hash) and are individually flagged with arrows at the top of the plot. The length of each arrow is an indicator of the strength of $70\ \mu\text{m}$ excess relative to the stellar photosphere. There is no correlation between metallicity and the detection of IR excess.

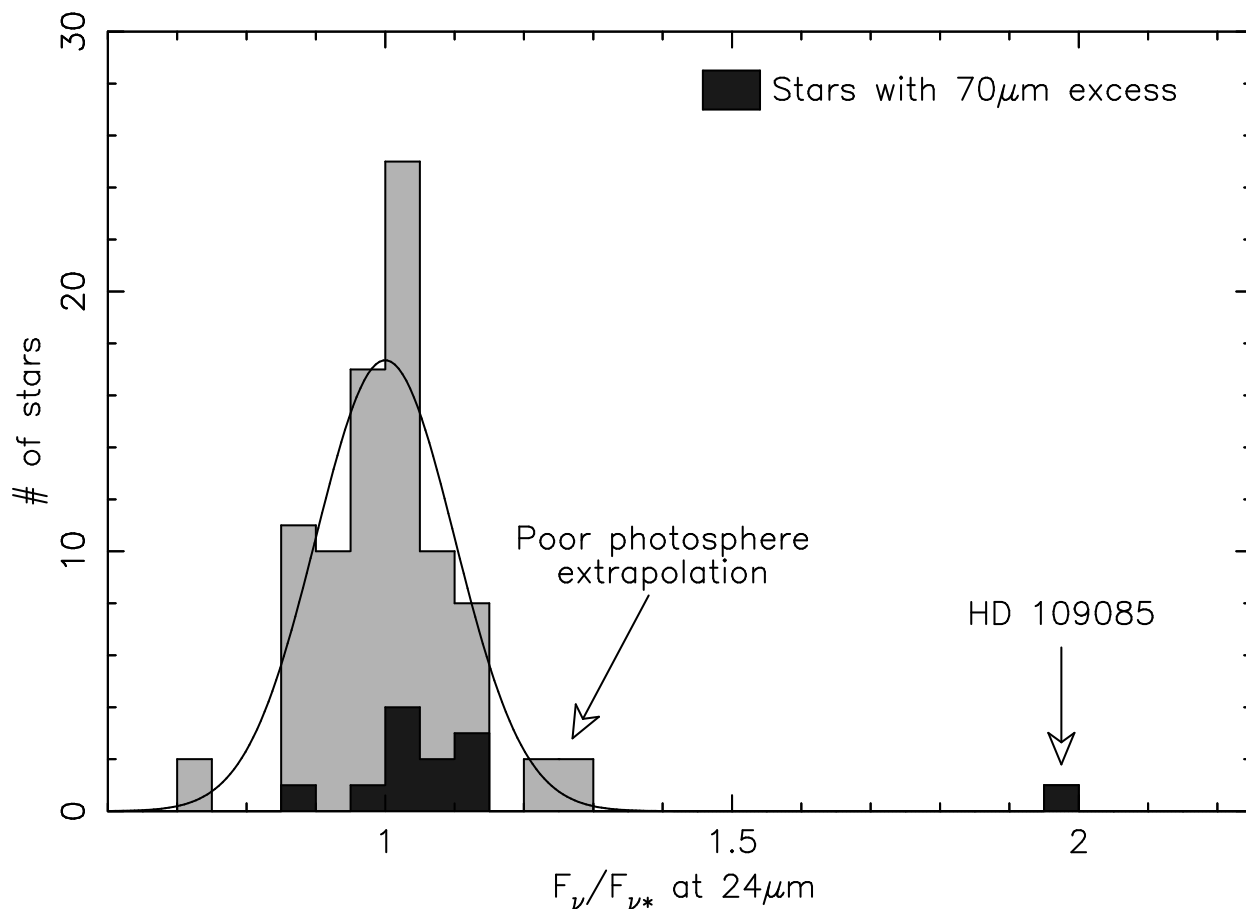


Fig. 4.— Distribution of $24\ \mu\text{m}$ fluxes relative to the expected photospheric values. A Gaussian distribution with 10% dispersion (*solid curve*) is shown for comparison. One star (HD 109085, a star previously identified as having excess emission) clearly stands out from the main population. The broad dispersion within this population is due to a variety of factors. Some stars have poor estimates of the stellar flux at $24\ \mu\text{m}$ due to poor near-IR data or photospheric models, particularly for the set of late K and M stars marked ‘poor extrapolation’ in the figure. The spread of values is also increased by sources with true, weak excesses (at the level of $\sim 10\%$ above the stellar photosphere). Stars with excesses at a longer wavelength ($70\ \mu\text{m}$) are shown with black shading.

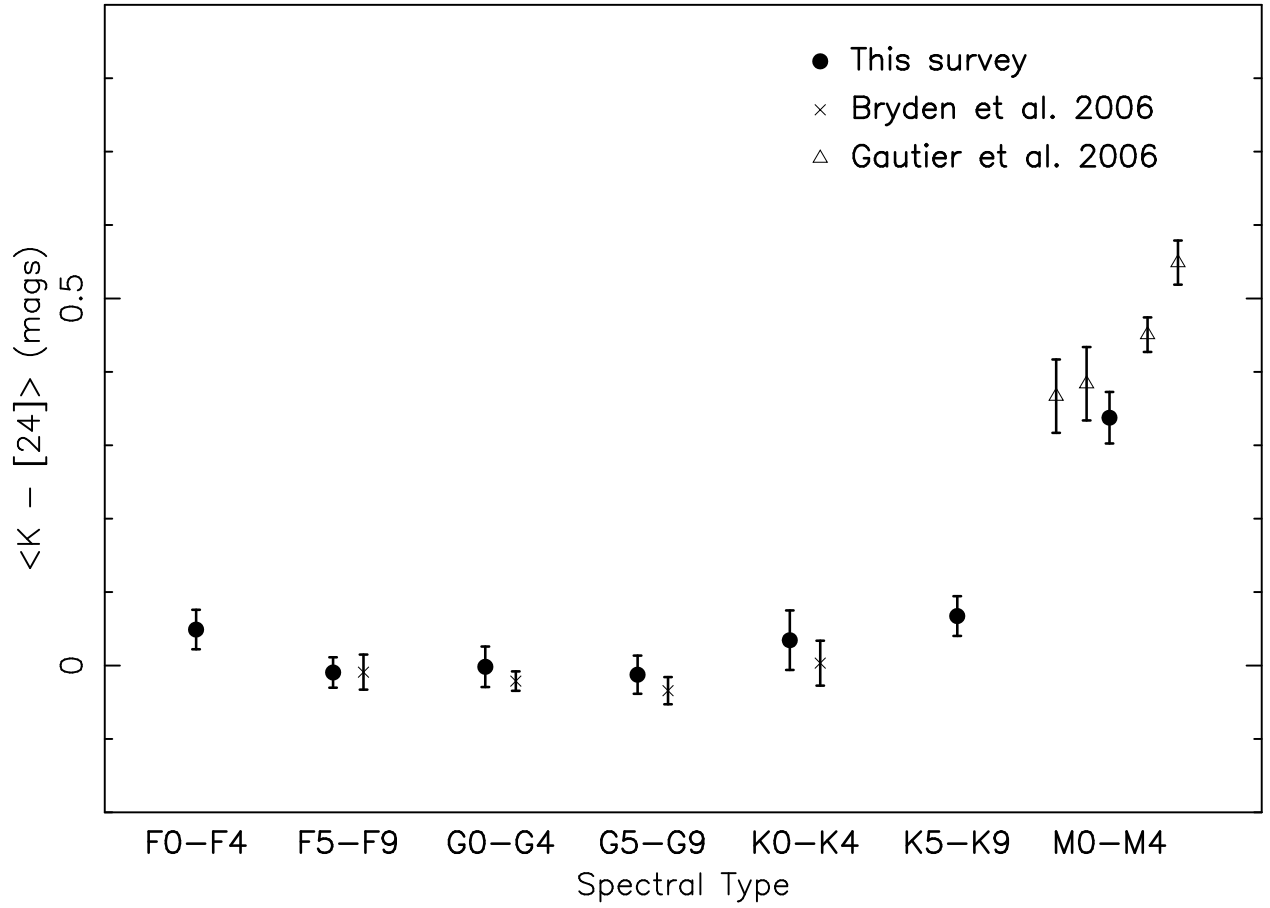


Fig. 5.— Average $24 \mu\text{m}$ color relative to 2MASS K_s band ($2.16 \mu\text{m}$) as a function of spectral type. Stars with excess emission or with poor K_s measurements are excluded. Error bars indicate the error on the mean value within each bin (not the overall dispersion). Stellar colors from the Bryden et al. (2006a) F5-K5 survey and the Gautier et al. (2006) M star survey are also shown for comparison. The trend is relatively flat over most of the range, with significantly red colors only seen among the M type stars.

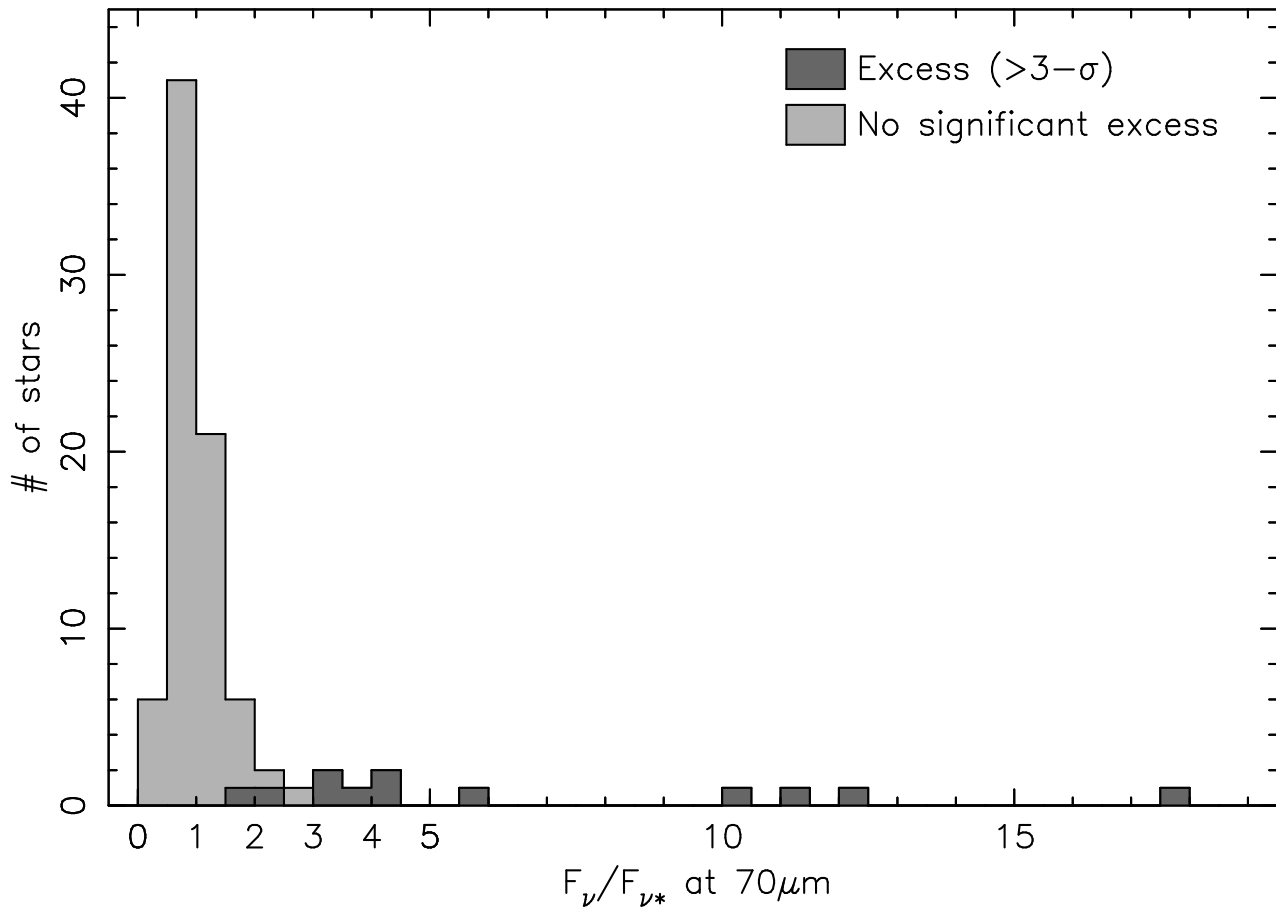


Fig. 6.— Distribution of $70\ \mu\text{m}$ fluxes relative to the expected photospheric values. While most stars cluster around unity (consistent with emission from the star alone) many show a high degree of excess emission attributable to circumstellar dust.

Fig. 7.— Composite image of the field surrounding HD 105211 (marked by a plus sign). In addition to our MIPS $24\ \mu\text{m}$ (green) and $70\ \mu\text{m}$ (red) images, the 2MASS K_s band image is overlaid in blue. While dim background stars show up as blue points, the cool Mira variable star CL Cru (triangle) has strong $24\ \mu\text{m}$ emission with a much broader PSF, resulting in an overall green color. This bright star contaminated the broad IRAS scanning beam (dashed yellow rectangle) prohibiting the detection of dust around HD 105211. In the MIPS image, HD 105211 is well resolved, showing strong excess emission at $70\ \mu\text{m}$. The neighboring star CPD-63 2145B (asterisk), while detected at $24\ \mu\text{m}$, does not give off significant emission at $70\ \mu\text{m}$.

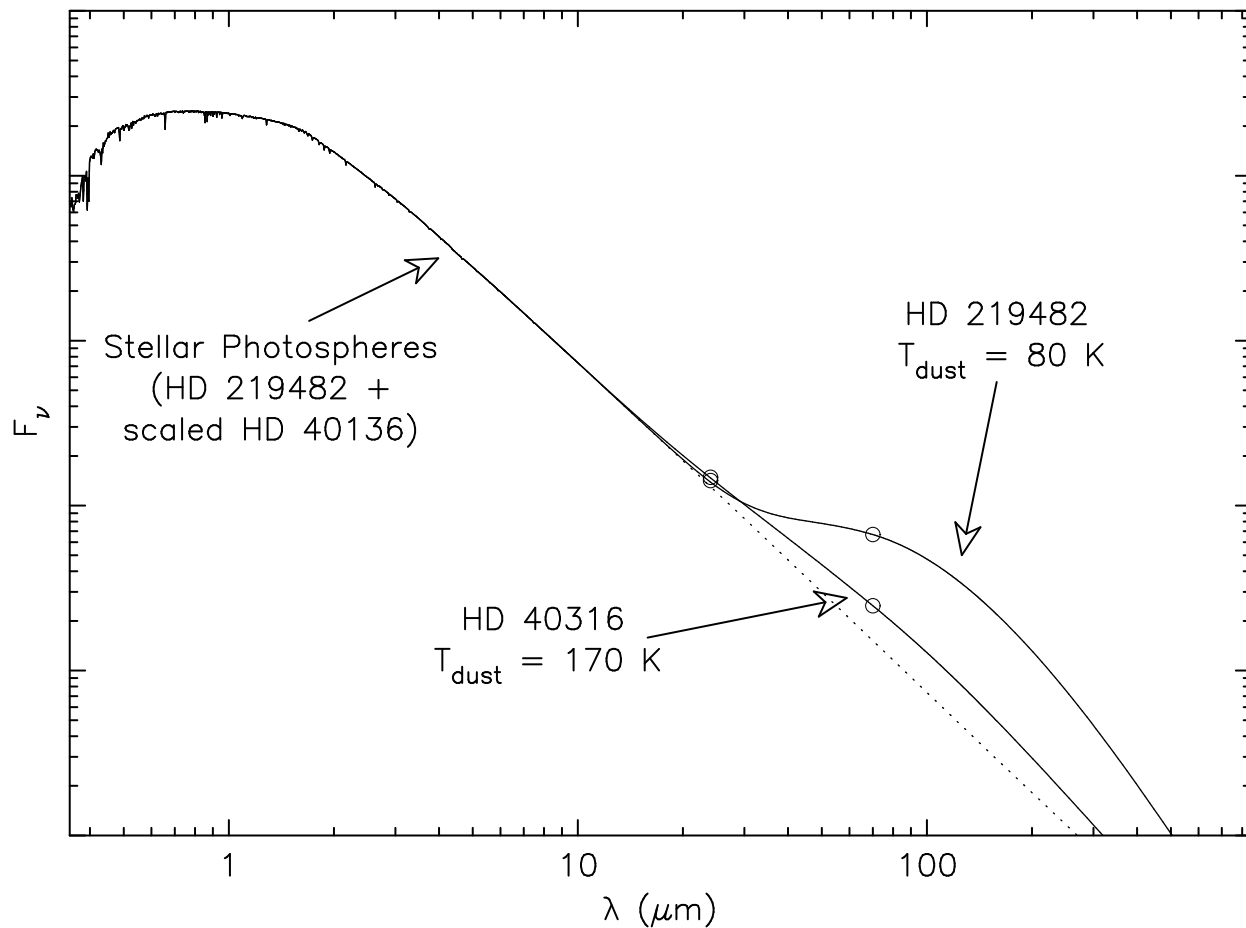


Fig. 8.— Spectral energy distributions for two stars with IR excess at both 24 and 70 μm . The emission from the two stars has been scaled such that their photospheres overlap, emphasizing the difference in far-IR emission. The observed fluxes at each wavelength are shown as open circles that are fit with a combination of emission from the stellar photosphere (*dotted line*) and from orbiting dust. The dust emission of HD 40316 is fit with 170 K dust, whereas HD 219482, with stronger 70 μm and weaker 24 μm emission, is fit with cooler, 80 K dust.

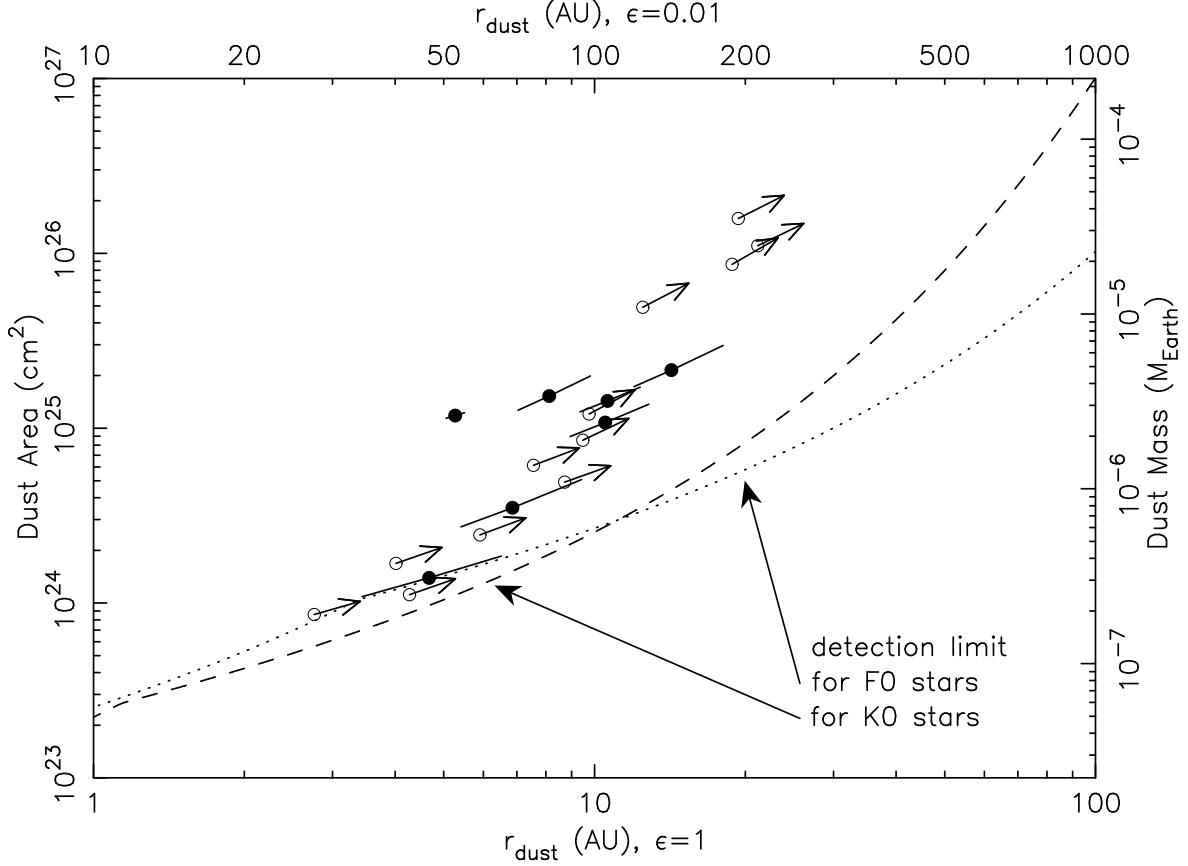


Fig. 9.— Area and dust mass estimates for stars with $70 \mu\text{m}$ excess emission. In addition to our 12 stars with excess, the 7 excess stars from Bryden et al. (2006a) are also shown. Dust temperatures (Table 4) are translated into orbital radii assuming either large blackbody grains (bottom axis) or small grains with emissivity 0.01 (top axis). Stars with excess measured at both 24 and $70 \mu\text{m}$ are shown as solid points, while those with only upper limits for the dust temperature are shown as open circles. Error bars are added to each point based on the $1\text{-}\sigma$ uncertainties in the dust temperature; for systems with upper limits on the dust temperature, an arrow is plotted with length/direction based on an assumed 10% uncertainty in the temperature. Dust masses (right axis) are calculated assuming a typical grain size of $10 \mu\text{m}$. Both dust area and mass are calculated under the assumption of blackbody grains (unity emissivity); for an emissivity of 0.01, both area and mass are a factor of 100 larger. The detection limits, which depend on the stellar temperature, are shown for a F0 star (dotted line) and for a K0 star (dashed line).

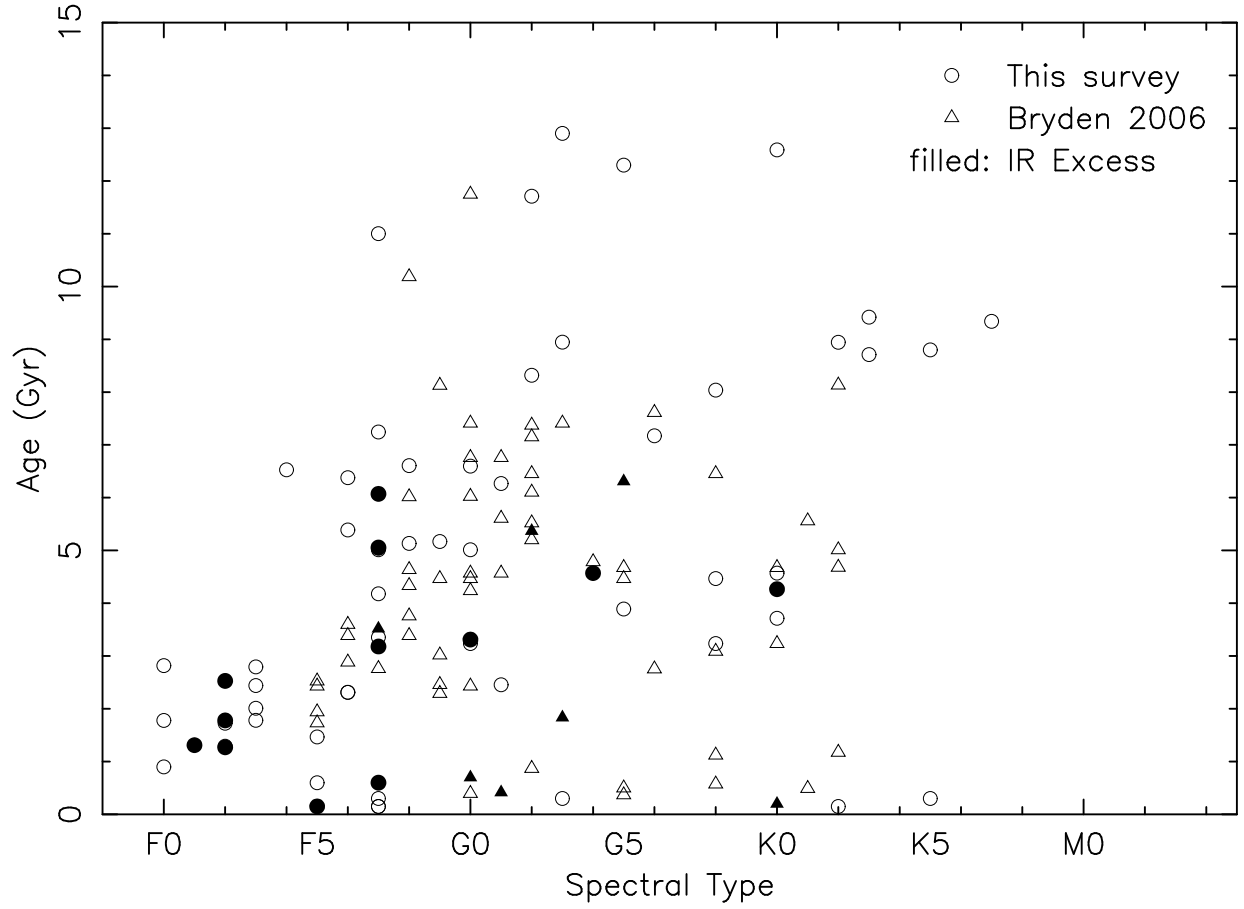


Fig. 10.— Stellar age as a function of spectral type for stars with known ages. The stars from this survey are marked with circles, while those from Bryden et al. (2006a) are marked as triangles. In both cases, stars with IR excess are marked as filled symbols.

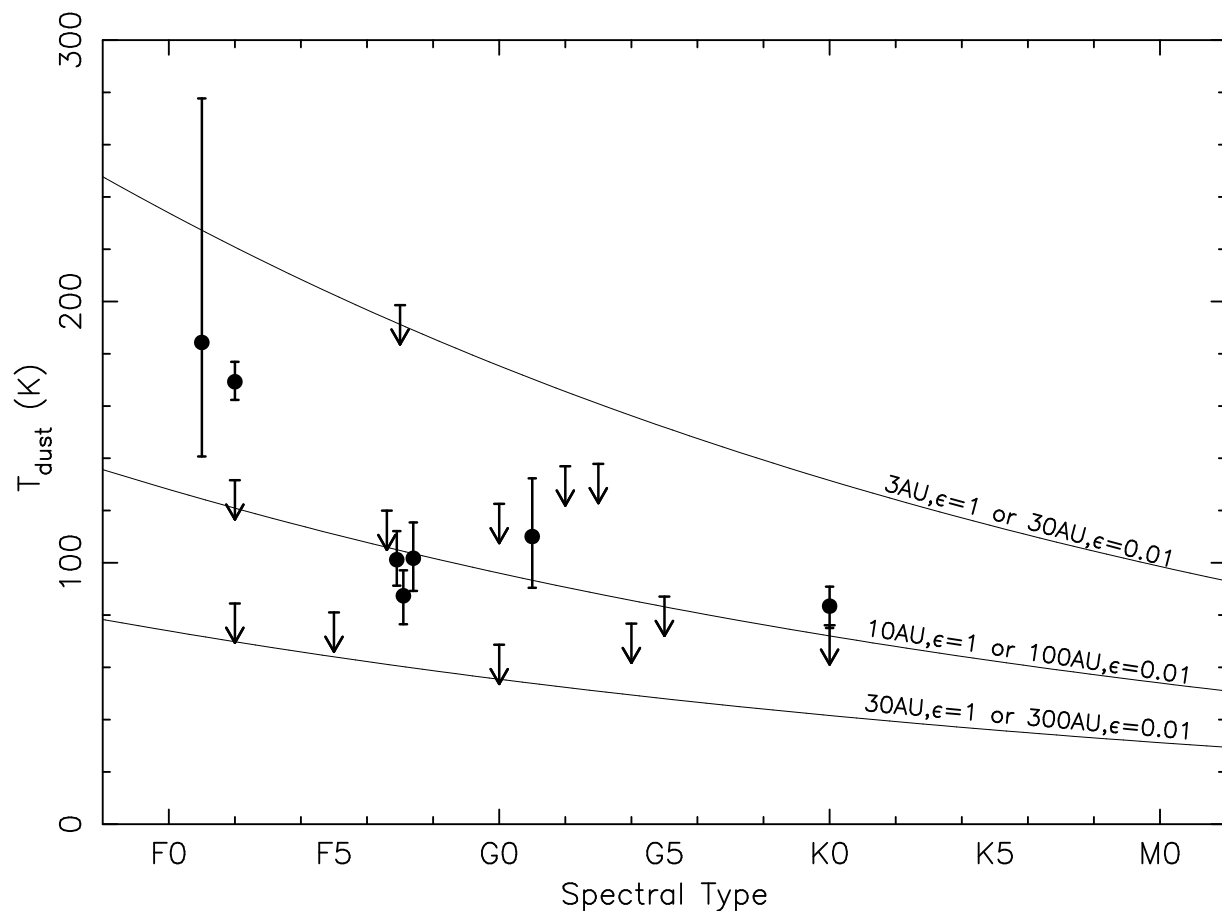


Fig. 11.— Dust temperature for stars with IR excess in this sample and from Bryden et al. (2006a). For stars with excess measured at both 24 and 70 μm (solid points), the dust SED is fit with a representative temperature. Those stars with a single measurement of excess at 70 μm only have ($3\text{-}\sigma$) upper limits. With some assumptions for the grain properties, the dust temperatures can be translated to orbital distances. Several lines of constant distance are shown for comparison. The observed systems with measured dust temperatures are mostly consistent with large blackbodies orbiting at ~ 10 AU or small, low-emissivity grains at ~ 100 AU. There is no clear evidence for orbital distance changing as a function of spectral type.

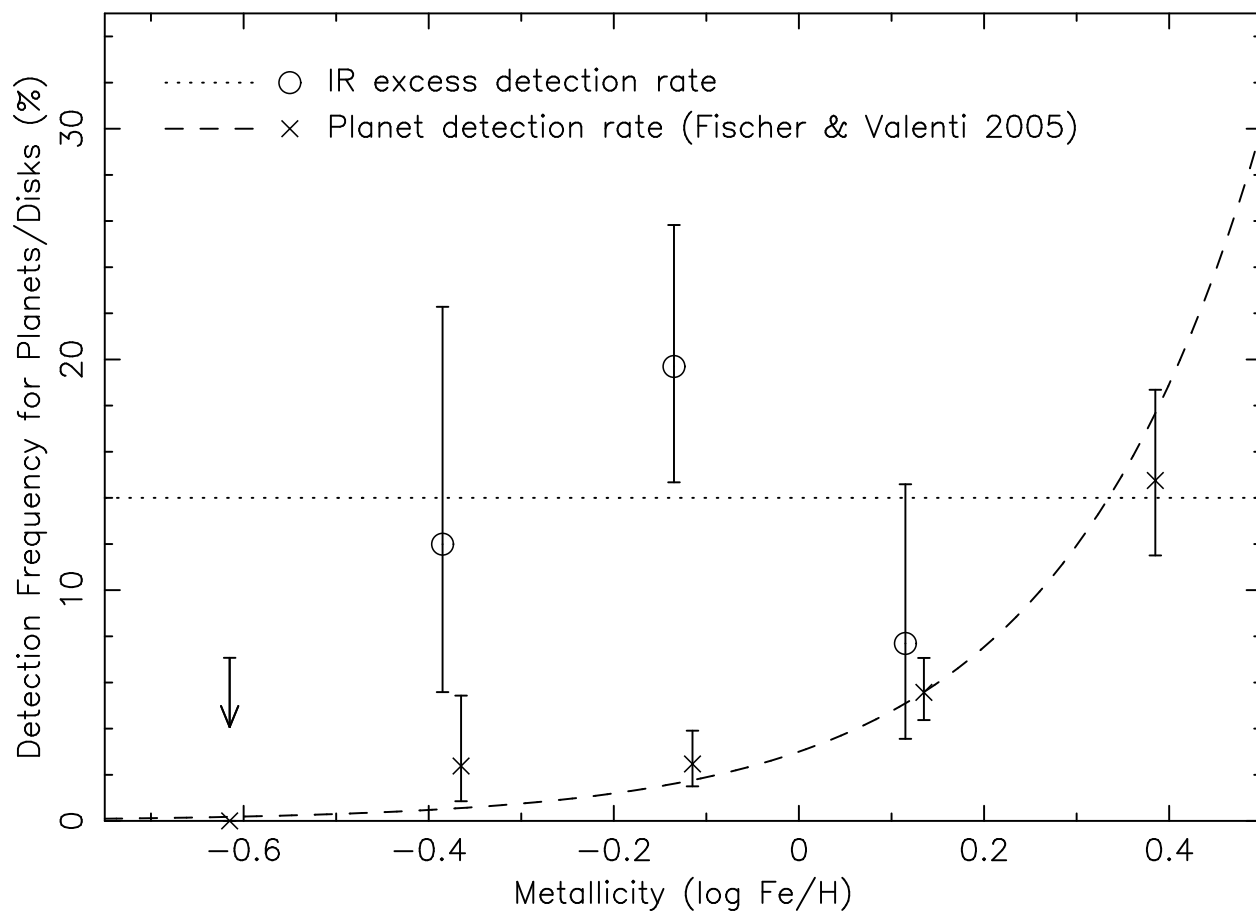


Fig. 12.— Detection frequency of planets and IR excess as a function of stellar metallicity. For the stars presented in this paper, plus those of Bryden et al. (2006a), the detection rate of $70 \mu\text{m}$ excess emission is shown as open circles. The distribution has no trend in metallicity; all points are consistent with the average detection rate for the entire sample (14%; dotted line). This is in contrast to the dependence of the planet detection rate on metallicity for a similar sample of nearby stars (x marks), which Fischer & Valenti (2005) fit with a metallicity-squared relationship (dotted line).

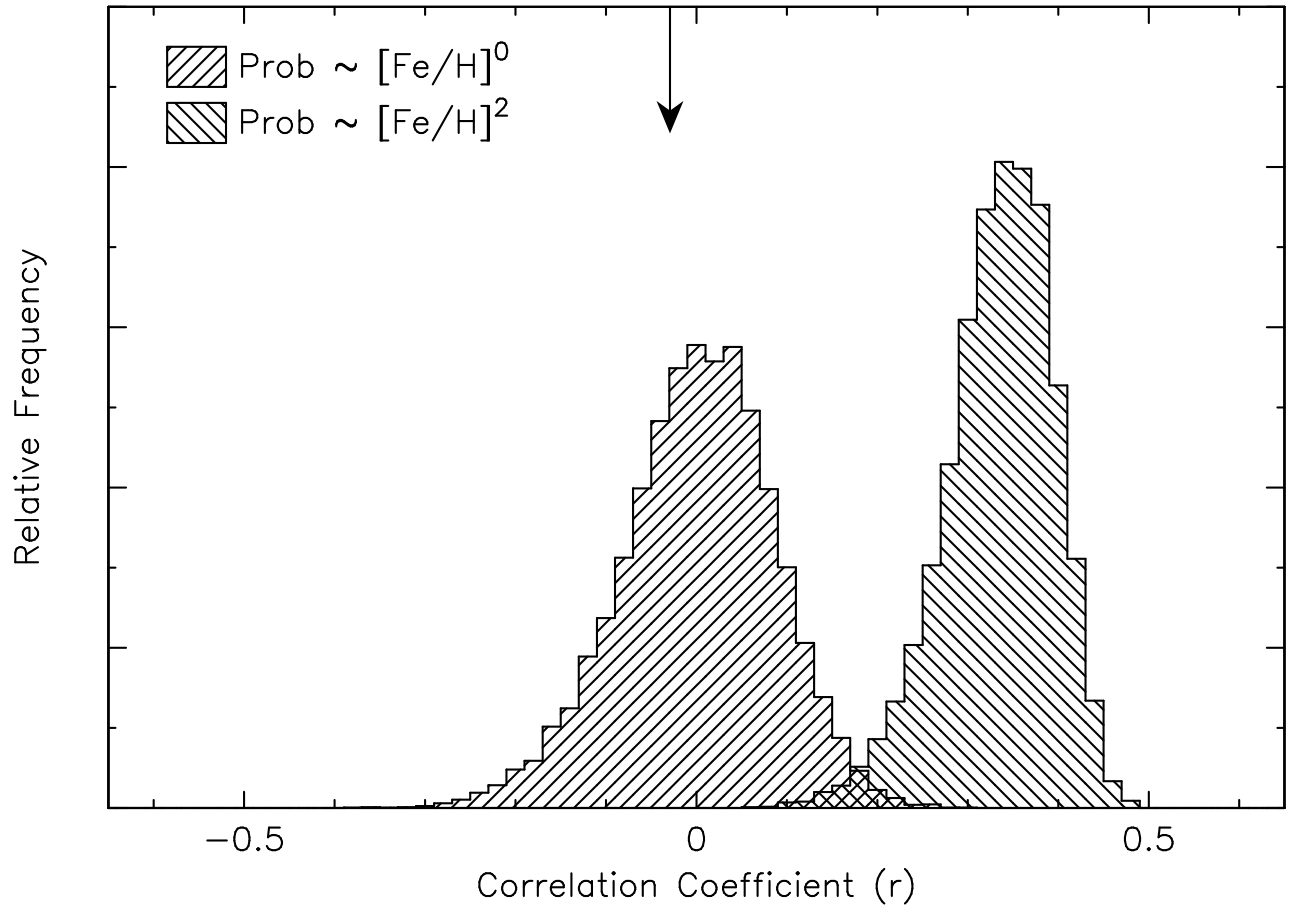
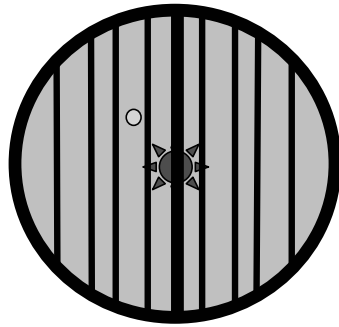
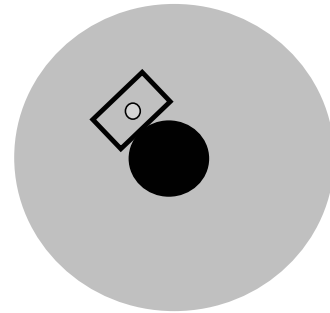


Fig. 13.— Distribution of r correlation coefficients for two series of monte carlo simulations. Stars were selected either completely randomly (left histogram) or proportionate to their metallicity squared (right histogram), the relationship observed for planet-bearing stars. The arrow at the top shows the value of r observed within our data, strongly inconsistent with the planet-metallicity relationship.



Infrared Interferometer

$r=0.5''$ beam or
5 AU at 10 pc



Visible Coronagraph

$0.039'' \times 0.017''$ beam or
 0.4×0.17 AU at 10 pc

Fig. 14.— The interferometer (*left*) takes in all emission from a face-on exo-zodiacal disk that fits within the diffraction-limited beam of a single telescope. The intensity is, however, attenuated by the interferometric fringe pattern shown as vertical black bars. The coronagraph (*right*) takes in exo-zodiacal light only within the area of a single diffraction-limited pixel; the values shown here are appropriate for a 3.5x8 m telescope under consideration for TPF-C.

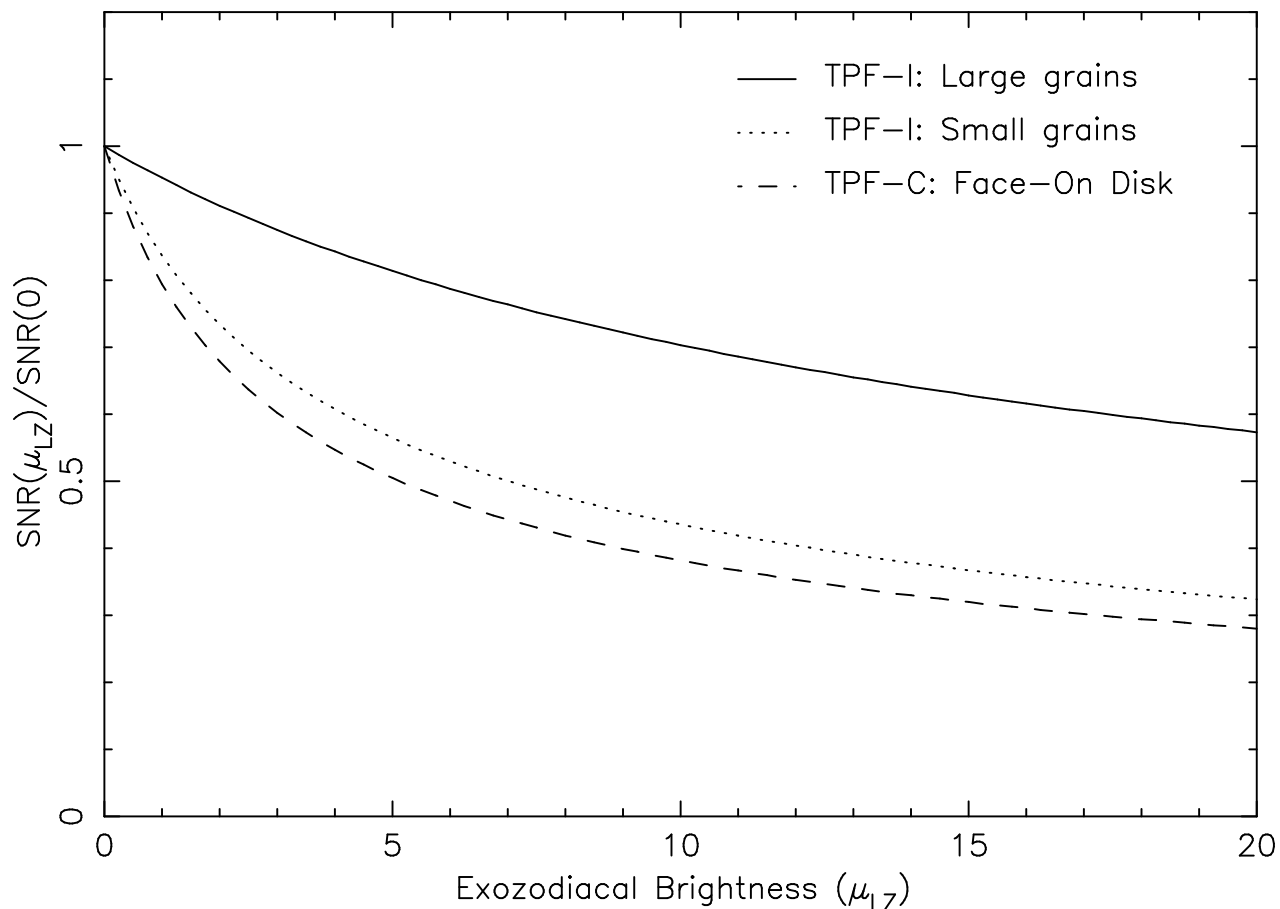


Fig. 15.— The effect of exo-zodiacal dust emission on TPF signal-to-noise ratio. The horizontal axis gives the vertical optical depth of the exo-zodiacal disk normalized to that of the Solar System (μ_{LZ}). Note that a value of $\mu_{EZ} = 1$ in a target system corresponds to twice the emission we see from our zodiacal cloud, e.g. using COBE or IRAS, since we view our cloud from its midplane. The upper two curves show the falloff in relative S/N for the interferometer as the amount of exo-zodiacal emission increases, with large and small grain sizes considered separately (solid and dotted lines respectively). The lower curve (dashed line) shows a similar trend for a coronagraph viewing a face-on disk. In each case, the signal-to-noise ratio is shown relative to observations of a system with no dust emission.